RESEARCH ARTICLE

Key Points:
- A numerical approach is introduced to perform Von Neumann linearized analysis on high-order methods with complex time-marching schemes
- A new set of test cases can demonstrate the dispersion and dissipation properties of numerical schemes and are validated against the linearized analysis
- The advantages and disadvantages due to grid staggering choices—such as better phase speed prediction or stronger time step restrictions—diminish with high-order schemes

Correspondence to:
X. Chen,
xic@princeton.edu

Towards an Unstaggered Finite-Volume Dynamical Core With a Fast Riemann Solver: 1-D Linearized Analysis of Dissipation, Dispersion, and Noise Control

Xi Chen[1,2] , **Shiann-Jiann Lin[2]**, and **Lucas M. Harris[2]**

[1]Program in Atmospheric and Oceanic Sciences, Princeton University, Princeton, NJ, USA, [2]Geophysical Fluid Dynamics Laboratory, NOAA, Princeton, NJ, USA

Abstract Many computational fluid dynamics codes use Riemann solvers on an unstaggered grid for finite volume methods, but this approach is computationally expensive compared to existing atmospheric dynamical cores equipped with hyper-diffusion or other similar relatively simple diffusion forms. We present a simplified Low Mach number Approximate Riemann Solver (LMARS), made computationally efficient through assumptions appropriate for atmospheric flows: low Mach number, weak discontinuities, and locally uniform sound speed. This work will examine the dissipative and dispersive properties of LMARS using Von Neumann linearized analysis to the one-dimensional linearized shallow water equations. We extend these analyses to higher-order methods by numerically solving the Fourier-transformed equations. It is found that the pros and cons due to grid staggering choices diminish with high-order schemes. The linearized analysis is limited to modal, smooth solutions using simple numerical schemes, and cannot analyze solutions with discontinuities. To address this problem, this work presents a new idealized test of a discontinuous wave packet, a single Fourier mode modulated by a discontinuous square wave. The experiments include studies of well-resolved and (near) grid-scale wave profiles, as well as the representation of discontinuous features and the results are validated against the Von Neumann analysis. We find the higher-order LMARS produces much less numerical noise than do inviscid unstaggered and especially staggered schemes while retaining accuracy for better-resolved modes.

1. Introduction

In modern dynamical core development, finite-volume schemes have become popular for atmospheric transport due to inherent conservation property and better physical consistency, since many physical parameterizations assume that the inputs are volume-mean variables rather than point based. In many CFD applications, the finite-volume method is applied on a unstaggered grid using an approximate Riemann solver to calculate the volume interface fluxes. Traditional Riemann solvers, such as Roe (Roe, 1981), HLL (Harten et al., 1997), and AUSM+-up (Liou, 2006) solvers, provide implicit diffusion for a large range of applications of different Mach numbers. However, compared to geophysical dynamical cores, the mathematical formulation of these solvers are complicated and computationally expensive. Additionally, in contrary to traditional Riemann solver-based approaches, dynamical cores developed for geophysical flows are usually discretized on different grid staggering choices (see Arakawa & Lamb, 1977, for the definition of A-, B-, C-, and D-Grid). Although the traditional Riemann solver-based approach can be expensive, it has unique advantages in an atmospheric application. First, simulations using a Riemann solver can achieve implicit high-order diffusion, thus permitting sharper results with less smearing. Second, using unstaggered variables makes it straightforward to couple dynamics with physical parameterization because the velocity components are colocated with scalars (density, tracers, temperature, etc.). Finally, the vector wind is readily available and thus flexible to manipulate. On an unstaggered grid, it is easier and more accurate to perform horizontal vector interpolation, project wind components into different local coordinates, or to calculate the 3-D Coriolis force needed in deep-atmospheric dynamics. Therefore, despite performance difficulties, in recent years, many efforts have been made to implement the unstaggered Riemann solver for atmospheric applications (Abdi & Giraldo, 2016; Giraldo & Restelli, 2008; Katta et al., 2014; Kelly & Giraldo, 2012; Kopera & Giraldo, 2014; Ullrich et al., 2010; Ullrich & Jablonowski, 2012; Yang et al., 2010).

The disadvantage in speed is one of the leading hurdles of a Riemann solver-based dynamical core to be used in geophysical fluid applications. The Rusanov approximate Riemann solver is one exception with competitive computational efficiency, but it is excessively diffusive compared to other carefully designed approximate Riemann solvers such as Roe, and AUSM+up (Ullrich et al., 2010). Indeed, geophysical flows are much more manageable to simulate than many high-energy flows since the supersonic, vacuum, and rarefaction flows are absent. To address this issue, Chen et al. (2013) introduced a Low Mach number Approximate Riemann Solver (LMARS) with simple mathematical expressions, owing to a series of assumptions appropriate for the atmospheric flows: low speed compared to the acoustic waves, weak discontinuities, and locally uniform sound wave speed. LMARS makes it possible to build a dynamical core that benefits from the Riemann solvers while keeping comparable computational efficiency to many state-of-the-art dynamical cores. This work is the first in a series to explore the unstaggered finite-volume method implementation with the LMARS within the FV3 (Finite-Volume Cubed-Sphere Dynamical Core) framework (Harris & Lin, 2013; Harris et al., 2016; Lin & Rood, 1996; Lin, 2004). This work will give the derivation of the Riemann solver with linearized shallow water equations. It will be demonstrated that in the linearized formulation, the implicit diffusion introduced by the Riemann solver is equivalent to an explicitly added high-order diffusion.

Another possible reason that Riemann solver-based schemes are not well received in geophysical applications is the concern of using on unstaggered grid. Historically, in numerical weather prediction and climate simulation, the unstaggered grid is considered a poor choice because it is believed to have significant dispersion errors for short wavelength modes. Traditional linearized analysis shows the unstaggered schemes have the worst performance in resolving the grid-scale processes because such waves are almost stationary. However, such conclusions usually are drawn from the analysis of low-order and inviscid simplified schemes; the properties of high-order schemes are underexplored. Therefore, it is natural to perform the Von Neumann analysis on high-order LMARS to examine if any adverse dispersion property suggested by the traditional perception exists. In the context of the geophysical flows, several previous works have conducted linearized analyses of high-order numerical schemes in 1-D and 2-D (Eldred & Le Roux, 2018; Giraldo, 2014; Kent et al., 2014; Lauritzen, 2007; Randall, 1994; Skamarock, 2008; Staniforth et al., 2013; Ullrich, 2014). Due to the complexity of the high-order scheme, many authors have simplified the flow properties, for example, constant flow, and others have neglected high-order terms in the numerical schemes, which might have significant impact on the dispersive or dissipative properties. Some analysis leveraged the modern computer program to solve the algebraic equations but went into the out-of-precision-limit problem due to the complexity of the high-order schemes. Moreover, other factors, particularly time discretization, upwinding, and nonlinear effects, are largely ignored in these analyses. It is unclear if results on low-order inviscid schemes can be generalized to real-world models. Some recent attempts have been made to better incorporate these factors in linearized analysis. In particular, Ullrich (2014) systematically analyzed several high-order 1-D explicit methods using a numerical approach to perform the linearized analysis. Kent et al. (2014) applied this method to investigate the roles of more numerical components, such as diffusion terms and time-marching schemes to the dissipative-dispersive relations. This work follows the numerical analyses of Ullrich (2014) and of Kent et al. (2014) and focuses on the role of the grid staggering choices to both dispersion and dissipation properties of high-order schemes and how the diffusion mechanisms alter them. One advancement is to enable linearized analyses to treat implicit terms in implicit or semi-implicit methods, such as the forward-backward (FB) time-stepping scheme (Mesinger, 1977). This numerically discretized analysis approach could be useful to other numerical procedures with more sophisticated time marching or stepping schemes by iterating the approaches introduced in this work. This numerical approach, denoted by "numerical Von Neumann analysis," circumvents the burden of the algebraic derivation of high-order discretization by discretizing the solutions of the Von Neumann analysis into the 2-D space of Courant numbers and numerical phase. The linearized shallow water environment is chosen to test the algorithms because it allows the reference solutions to have constant group velocities, and because it is a coupled system that makes it possible to use a FB time scheme to achieve a single-time-step high-order method. The following sections will show that the differences based on grid staggering choices will diminish for schemes with higher-order accuracy in spatial discretization. It will also prove that the diffusion terms in the discretization alter both dispersion properties and Courant number restrictions significantly. Therefore, results based on simplified Von Neumann analysis by neglecting diffusion terms cannot be generalized.

The primary goal of this work is to find the capabilities or limitations of LMARS to represent the small-scale waves in a closer-to-real-world environment. Although the linearized analysis is a powerful tool, it has many

limitations. First, the analysis can only apply to smooth solutions. Large-scale atmospheric flows, such as planetary waves, are smooth compared to other CFD applications, such as high-energy shocks. However, mesoscale flows can contain sharp gradients, such as fronts, which can generate high-frequency noise. Therefore, the ability to handle discontinuities without creating numerical noise becomes increasingly essential as model resolution increases. The linearized analysis cannot explicitly demonstrate the model's ability to handle discontinuities and other nonmodal features. Second, although the dissipation and dispersion errors can be separately calculated, their interaction is difficult to analyze, and most of the time diffusive effects are overlooked. To address these two issues, a simple-to-setup test case is designed that can reveal both the combined dissipative-dispersive properties and the noise control of a numerical scheme. This numerical test suite is designed similarly to the ones described in Staniforth et al. (2013), but much more challenging. The new test can expose some weakness from some inviscid numerical schemes demonstrating that inviscid methods are not suitable for high-resolution geophysical applications. The results of the tests are proved consistent with the theoretical linearized analysis in smooth tests. The nonsmooth tests visualize the numerical scheme's ability to treat the noise due to weak discontinuities. It is found that when nonlinear effects such as filtering noise have to be considered in the algorithm design, the poor dispersion properties at grid-scales are insignificant and designing proper diffusion is more important. It will be shown that the high-order LMARS has an optimum automatically generated matching dissipation and dispersion curves.

This work is organized as follows. Section 2 exhibits our core algorithms, including the linearized LMARS and the spatial and temporal discretization. In section 3, both analytical and numerical approaches to perform the Von Neumann linearized analysis will be presented. The newly designed tests will be illustrated in section 4. This work is concluded in section 5. Further supporting information is contained in Appendix A.

2. Discretization of the 1-D linearized Shallow Water Equations

2.1. The Linearized Shallow Water Equations

The linearized one-dimensional shallow water equations are

$$\frac{\partial \phi}{\partial t} = -gH\frac{\partial u}{\partial x} \tag{1}$$

$$\frac{\partial u}{\partial t} = -\frac{\partial \phi}{\partial x} \tag{2}$$

where ϕ is the geopotential height, H the reference flow height, u the flow speed, and g the acceleration due to gravity. By eliminating u, it can be found

$$\frac{\partial^2 \phi}{\partial t^2} = gH\frac{\partial^2 \phi}{\partial x^2} = a^2 \frac{\partial^2 \phi}{\partial x^2} \tag{3}$$

where $a = \sqrt{gH}$ is the nondispersive group velocity or the gravity wave speed.

This system has analytic solutions:

$$\hat{\phi} = \hat{\phi}_k e^{i(kx \pm akt)} \tag{4}$$

$$\hat{u} = \mp \frac{1}{a}\hat{\phi}_k e^{i(kx \pm akt)} \tag{5}$$

Note that the waves propagate in both directions, which is similar to the nonlinear shallow water physics. However, the linearization constrains the group velocity to a constant value, which is helpful when performing the dispersion analysis on different numerical schemes.

2.2. LMARS With Linearized Shallow Water Equations

In the classical work, Godunov (1959) presented the first conservative upwind scheme to a nonlinear systems of conservation laws, and the first solution of a Riemann problem in a finite volume context. The Riemann problem's solution can be used locally in the method of Godunov and high-order extensions of it. Although there is no exact solution to the Riemann problem for the Euler equations, it is possible to find the exact solution to the linearized shallow water equations.

The full nonlinear compressible LMARS is derived in Chen et al. (2013). The equivalent expression in the linearized shallow-water dynamics can be analogously derived.
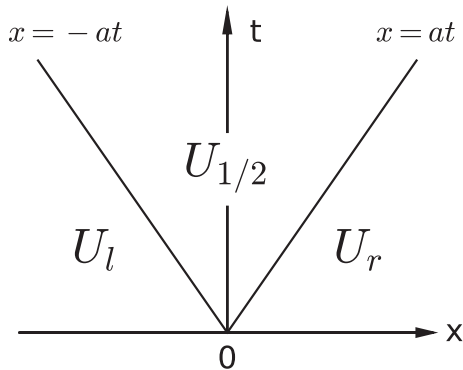
Figure 1. Structure of the solution of the Riemann problem on the $x - t$ plane for the 1-D time-dependent linearized shallow water equations.

Equations (1) and (2) can be written as a Riemann Problem:

$$U_t + \mathbf{A}U_x = 0 \tag{6}$$

where

$$U = \begin{bmatrix} \phi \\ u \end{bmatrix} \tag{7}$$

$$\mathbf{A} = \begin{bmatrix} 0 & a^2 \\ 1 & 0 \end{bmatrix} \tag{8}$$

with initial conditions

$$U(x, t = 0) = \begin{cases} U_l & x \leq 0 \\ U_r & x > 0 \end{cases} \tag{9}$$

This Riemann problem has two solutions, which are associated with the eigenvalues to $\mathbf{A}U = \lambda U$, $\lambda_{1,2} = \mp a$. The two waves separate three constant states (Figure 1).

Following the derivation of LMARS in Chen et al. (2013), denote the values of U to the left of the discontinuity as $U_l = [\phi_l, u_l]^T$, to the right as $U_r = [\phi_r, u_r]^T$, and at the interface as $U_{1/2} = [\phi_{1/2}, u_{1/2}]^T$. Then the Rankine-Hugoniot "jump" conditions (Hirsch, 2007) give

$$\lambda_1 \left(U_{1/2} - U_l \right) = \mathbf{A} \left(U_{1/2} - U_l \right) \tag{10}$$

$$\lambda_2 \left(U_{1/2} - U_r \right) = \mathbf{A} \left(U_{1/2} - U_r \right) \tag{11}$$

or:

$$\phi_{1/2} + au_{1/2} = \phi_l + au_l \tag{12}$$

$$\phi_{1/2} - au_{1/2} = \phi_r - au_r \tag{13}$$

Solving the system yields

$$\phi_{1/2} = \frac{1}{2} \left(\phi_l + \phi_r \right) + \frac{a}{2} \left(u_l - u_r \right) \tag{14}$$

$$u_{1/2} = \frac{1}{2} \left(u_l + u_r \right) + \frac{1}{2a} \left(\phi_l - \phi_r \right) \tag{15}$$

Since the group velocity of the system described by the linearized shallow water equations is a constant, the linearized LMARS is exact.

2.3. Naming Convention to Categorize Different Methods

It could be more conventional to use the formal order of accuracy to categorize different numerical methods. However, as pointed out in Chen et al. (2013), high-order one-dimensional discretizations might be still second-order accurate in a multidimensional scheme if the cross-terms are not included. Additionally, staggered and unstaggered schemes might involve different size stencils at the same order of accuracy. Instead, the minimum required ghost-cells in a doubly periodic domain, N_g, which results in comparable accuracy and complexity between different discretization methods. Therefore, albeit slightly subjective, the value of N_g is considered a consistent way to categorize different methods in this work. Since this work is restricted to one-dimensional problems, the terms N_g, "length of the computational stencil," or "order of accuracy" might be used interchangeably.

2.4. The Polynomial Interpolation-Based Spatial Discretization

The governing equations (1) and (2) can be numerically solved in a one-dimensional space. Let j be the domain mesh index, ranging from $-N$ to N with $x_j = j\Delta x$, where Δx is the grid spacing, the time step is Δt. The spatial discretization depends on grid staggering choices. In an unstaggered grid, the variables u_j and ϕ_j are defined at the same location, also called the colocated grid or A-Grid. In a staggered grid or C-Grid, the velocity u_j is located at the midpoint $x_{j-0.5}$ between two neighboring ϕ_{j-1} and ϕ_j. One of the advantages of the C-grid is that the gradient of u, $(\partial u/\partial x)_j$, is colocated with ϕ_j in a central differencing scheme. Although the goal is to seek an unstaggered grid approach for the new model, the pros and cons of these two grids will also be analyzed and served as the baseline.

Table 1
The Coefficient to Calculate "East" Side Midpoint Value on a Stencil Number
$N_c = 2N_g - 1$ From Point-Value Variables

N_g	$E_{pt}^{(-2)}$	$E_{pt}^{(-1)}$	$E_{pt}^{(0)}$	$E_{pt}^{(1)}$	$E_{pt}^{(2)}$
1			1		
2		−1/8	3/4	3/8	
3	3/128	−5/32	45/64	15/32	−5/128

The reconstructed distribution of the discretized variables is based on the polynomial interpolation. A generic variable at x_j is denoted η_j. To calculate the value at $x_{j+0.5}$, using a stencil of $N_c = 2N_g - 1$ points ($N_g = 1, 2, ...$), we write

$$\eta_j^E = \sum_{l=1-N_g}^{N_g-1} E^{(l)} \eta_{j+l} \tag{16}$$

The coefficient $E^{(l)}$ denotes the coefficient for the "east" neighbor midpoint, named η_j^E, to η_j. Obviously, $N_c = 1$, $N_g = 1$ results in the most basic scheme: a piecewise constant value reconstruction of variable η and $\eta_j^E = \eta_j$. Similarly, a "west" coefficient $W^{(l)}$ is

$$\eta_j^W = \sum_{l=1-N_g}^{N_g-1} W^{(l)} \eta_{j+l} \tag{17}$$

where

$$W^{(l)} = E^{(-l)} \tag{18}$$

If η_j is defined as the point value at location x_j, the values of coefficient $E_{pt}^{(l)}$ is listed in Table 1, where "pt" stands for "point value." If η_j is defined as the volume-mean value within the region $[x_{j-0.5}, x_{j+0.5}]$, the values of coefficient $E_{vm}^{(l)}$ is listed in Table 2, where "vm" stands for "volume mean." The values of $E^{(l)}$ are calculated from the polynomial interpolation.

Using odd numbered stencils could result in "mismatched" midpoint values at the same location. For example, η_j^E and η_{j+1}^W both are located at $x_{j+0.5}$, but could have different values. Figure 2 illustrates the mismatch created by the 3-point-stencil interpolations. A Riemann solver usually uses the mismatched values as the input. If a Riemann solver is not used, an even number stencil reconstruction scheme for midpoint values of η i:

$$\eta_{j+0.5}^M = \frac{1}{2} \left(\eta_j^E + \eta_{j+1}^W \right) = \sum_{l=1-N_g}^{N_g} M^{(l)} \eta_{j+l} \tag{19}$$

where

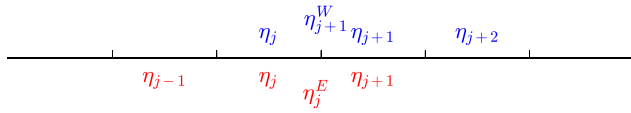$$M^{(l)} = \frac{1}{2} \left(E^{(l)} + W^{(l-1)} \right) \tag{20}$$

has the property

$$M^{(l)} = M^{(1-l)} \tag{21}$$

Similarly, $M^{(l)}$ has different values from point-value and volume-mean-value variables, namely, $M_{pt}^{(l)}$ and $M_{vm}^{(l)}$.

Table 2
The Coefficients to Calculate "East" Side Midpoint Value on a Stencil Number of
$N_c = 2N_g - 1$ From Volume-Mean Variables

N_g	$E_{vm}^{(-2)}$	$E_{vm}^{(-1)}$	$E_{vm}^{(0)}$	$E_{vm}^{(1)}$	$E_{vm}^{(2)}$
1			1		
2		−1/6	5/6	1/3	
3	1/30	−13/60	47/60	9/20	−1/20

Figure 2. At $x_{j+0.5}$, odd numbered stencil polynomial interpolation can create mismatched values. η_j^E is calculated from $\eta_{j-1}, \eta_j, \eta_{j+1}$, and η_{j+1}^W is calculated from $\eta_j, \eta_{j+1}, \eta_{j+2}$. The red and blue color indicate the required cells to calculate values to the left (red) and right (blue) to the cell interface at $i+0.5$.

Once the reconstructed coefficients $E^{(l)}$, $W^{(l)}$ and $M^{(l)}$ are derived, we may compute the coefficients of the spatial derivatives. In a grid-point scheme, such as a finite-difference method, the spatial derivative of a variable η can be evaluated by

$$\left(\frac{\partial \eta}{\partial x}\right)_j = \frac{1}{\Delta x}\sum_{l=-N_g}^{N_g} A_{pt}^{(l)}\eta_{j+l} = \left.\frac{\partial \eta}{\partial x}\right|_j + O(\Delta x^{2N_g}) \tag{22}$$

with a stencil of N_c points, $N_c = 1 + 2N_g$ in an unstaggered grid, and $N_c = 2N_g$ in a staggered grid.

The finite volume approach integrates the governing equation within a control volume, and the spatial derivative is written from the divergence theorem, projected in 1-D. The volume-mean value of the spatial derivative is

$$\left(\frac{\partial \eta}{\partial x}\right)_j = \frac{1}{\Delta x}\int_{x_{j-0.5}}^{x_{j+0.5}} \frac{\partial \eta}{\partial x}dx = \frac{1}{\Delta x}\left(\eta_{j+0.5} - \eta_{j-0.5}\right) \tag{23}$$

where the volume interface values $\eta_{j\pm0.5}$ needs to be evaluated. In fact, for unstaggered grid schemes, if $M_{vm}^{(l)}$ is used to evaluate $\eta_{\pm0.5}$, the coefficients of the derivatives with the finite volume method in equation (23) are identical to the ones derived using equation (22), and both methods would achieve $O(\Delta x^{2N_g})$ accuracy:

$$A_{pt}^{(l)} = A_{vm}^{(l)} = M_{vm}^{(l)} - M_{vm}^{(l+1)} = A^{(l)} \tag{24}$$

which also satisfies

$$A^{(l)} = -A^{(-l)} \tag{25}$$

This conclusion is not surprising, because achieving $O(\Delta x^{2N_g})$ accuracy specifies a unique $1 + 2N_g$ stencil.

Note that in the staggered grid approaches, the coefficients of $A^{(l)}$ are different and denoted by $A_c^{(l)}$. Additionally, using a Riemann solver in a finite volume method produces additional diffusion terms. These scenarios will be discussed in the following sections.

2.5. The FB Temporal Discretization

In the linearized shallow water equations (1) and (2), u and ϕ are coupled. The following FB time-stepping scheme is implemented:

$$\frac{\phi^{n+1} - \phi^n}{\Delta t} = \text{RHS}_h(u^n, \phi^n) \tag{26}$$

$$\frac{u^{n+1} - u^n}{\Delta t} = \text{RHS}_u(\phi^{n+1}, u^n) \tag{27}$$

where RHS stands for the numerical discretization of the right-hand side of equations (1) and (2). The FB unstaggered finite-volume scheme can be written:

$$\frac{\phi^{n+1} - \phi^n}{\Delta t} = -\frac{gH}{\Delta x}\left(u_{j+0.5}^n - u_{j-0.5}^n\right) \tag{28}$$

$$\frac{u^{n+1} - u^n}{\Delta t} = -\frac{1}{\Delta x}\left(\phi_{j+0.5}^{n+1} - \phi_{j-0.5}^{n+1}\right) \tag{29}$$

The numerical discretization will be revisited in the following sections with more generic forms. An example of the FB application in the real atmospheric simulation can be found in Lin (2004). Weller et al. (2013) also demonstrated better numerical stability with the FB schemes. Alternatively, one can also first update u^n to the next time step u^{n+1} and use u^{n+1} to update the geopotential height from ϕ^n to ϕ^{n+1}, but the overall effect is comparable.

It is worth noting that the FB time-stepping scheme is crucial because it provides extra implicit diffusion to the overall numerical scheme, yet only requires a single time level calculation. Otherwise, the explicit forward-Euler central differencing approach is unconditionally unstable for high order schemes (even with

extra diffusion provided by a Riemann solver, see Ullrich, 2014). For stability, a multistep time scheme, such as Runge-Kutta 3 or 4, is required for the explicit sub-step schemes (Ullrich, 2014). In the following sections, it will be shown that directly implementing the polynomial-interpolated derivatives with this temporal discretization would be inviscid or diffusive-error free, which would be ideal for dispersion error analysis. Other numerical schemes such as leap-frog scheme can also achieve similar results, but, it requires the solutions of two previous time-level states to calculate the next time level solutions. Without the additional requirement of explicit diffusion terms, the numerical discretization introduced in this section is of optimum complexity for a linearized shallow-water system.

3. A Numerical Approach to the Von Neumann Analysis

The Von Neumann analysis is a powerful tool to check stability, dissipative and dispersive errors of linearized schemes with periodical boundary conditions. The standard Von Neumann analysis is not reviewed since it can be found in various textbooks. The numerical approach to the Von Neumann analysis follows the naming convention of Hirsch (2007).

For the cleaner index expression, in any linear numerical scheme, the variables (ϕ_j, u_j) in the unstaggered grid are defined at location (x_j, x_j) and are defined at location $(x_j, x_{j-0.5})$ in the staggered grid. The update from time step n to $n + 1$ can be represented by the relation

$$\sum_l L^{(l)} \begin{bmatrix} \phi \\ u \end{bmatrix}_{j+l}^{n+1} = \sum_l R^{(l)} \begin{bmatrix} \phi \\ u \end{bmatrix}_{j+l}^{n} \tag{30}$$

where both $L^{(l)}$ and $R^{(l)}$ are 2 by 2 coefficient matrix for variables at location $j + l$.

On the finite mesh defined in section 2.4, $N + 1$ harmonics can be represented with their associated wave number k_m:

$$k_m = m \frac{\pi}{N \Delta x}, \quad m = 0, \dots, N \tag{31}$$

and the shortest wavelength that can be represented is $2\Delta x$. Using Von Neumann analysis, the solution to a single wave of wave number k at time level n can be written as follows:

$$\begin{bmatrix} \phi \\ u \end{bmatrix}_j^n = \begin{bmatrix} \hat{\phi} \\ \hat{u} \end{bmatrix}_0 \exp(ijk_m\Delta x - i\omega n\Delta t) = \begin{bmatrix} \hat{\phi} \\ \hat{u} \end{bmatrix}_0 \exp(ij\theta - in\Phi) \tag{32}$$

where ω is the linear frequency and $\Phi = \omega\Delta t = \Phi_r + i\Phi_i$ is the complex linear phase. The phase angle is defined as $\theta = k_m\Delta x = m\pi/N$.

With amplification factor defined as $G = \exp(-i\Phi)$, the generalized numerical discretization can be rewritten as follows:

$$G \sum_l \left\{ L^{(l)} \exp(il\theta) \right\} \begin{bmatrix} \hat{\phi} \\ \hat{u} \end{bmatrix}_0 = \sum_l \left\{ R^{(l)} \exp(il\theta) \right\} \begin{bmatrix} \hat{\phi} \\ \hat{u} \end{bmatrix}_0 \tag{33}$$

Multiplying the reverse of the coefficient matrix on the left-hand side and denoting the matrix for the discretization as P

$$P = \left(\sum_l \left\{ L^{(l)} \exp(il\theta) \right\} \right)^{-1} \left(\sum_l \left\{ R^{(l)} \exp(il\theta) \right\} \right) \tag{34}$$

yields

$$G \begin{bmatrix} \hat{\phi} \\ \hat{u} \end{bmatrix}_0 = P \begin{bmatrix} \hat{\phi} \\ \hat{u} \end{bmatrix}_0 \tag{35}$$

The amplification factor G is the eigenvalue of the 2 by 2 matrix P. The coefficients of $L^{(l)}$ and $R^{(l)}$ are determined constants, so P can be evaluated both analytically and numerically. The dissipation and dispersion errors can be evaluated by the solutions to G. The dissipation error is defined by the ratio of the numerical and theoretical amplification amplitude:

$$\epsilon_v = \frac{|G|}{|\hat{G}|} = |G| = \exp(\Phi_i) \tag{36}$$

The dispersion error is

$$\epsilon_\phi = \frac{\Phi_r}{ak\Delta t} = \frac{\Phi_r}{c\theta} \tag{37}$$

where $\Phi_r = \arctan\left(-\Im(G)/\Re(G)\right)$, c is the signed Courant number $c = a\Delta t/\Delta x$.

The following sections will demonstrate both traditional analytical derivation and numerical solutions to the amplification factor G from P.

3.1. The Central Differencing Schemes on the Unstaggered Grid

Without using the Riemann solver, the numerical discretization of this scheme can be written as follows:

$$\phi_j^{n+1} = \phi_j^n - ac \sum_{l=-N_g}^{N_g} A^{(l)} u_{j+l}^n \tag{38}$$

$$u_j^{n+1} = u_j^n - \frac{c}{a} \sum_{l=-N_g}^{N_g} A^{(l)} \phi_{j+l}^{n+1} \tag{39}$$

where $A^{(l)}$ is defined in equation (24).

3.1.1. Analytical Solution of the Amplification Factor for the Low-Order Central Differencing Unstaggered Scheme

Here we carry out the traditional "analytical" Von Neumann analysis. To analytically derive the amplification factor G, the velocity update discretization equation (39) can be further rewritten as

$$
\begin{aligned}
u_j^{n+1} &= u_j^n - \frac{c}{a} \sum_{l=-N_g}^{N_g} A^{(l)} \left[\phi_{j+l}^n - ac \sum_{m=-N_g}^{N_g} A^{(l)} u_{j+m+l}^n \right] = \\
&u_j^n - \frac{c}{a} \sum_{l=-N_g}^{N_g} A^{(l)} \phi_{j+l}^n + c^2 \sum_{l=-N_g}^{N_g} A^{(l)} \sum_{m=-N_g}^{N_g} A^{(m)} u_{j+m+l}^n
\end{aligned}
\tag{40}
$$

denoting

$$C_{FB}^{(p)} = \sum_{l=-N_g}^{N_g} A^{(l)} A^{(p-l)} \tag{41}$$

are the coefficients to the implicit diffusion due to FB numerical scheme. A Taylor expansion shows that the $C_{FB}^{(l)}$ on any variable η satisfies

$$\frac{1}{\Delta x^2} \sum_{l=-2N_g}^{2N_g} C_{FB}^{(l)} \eta_{j+l} = \left. \frac{\partial^2 \eta}{\partial x^2} \right|_{x_j} + O(\Delta x^{2N_g}) \tag{42}$$

which indicates that *the FB numerical scheme is equivalent to an explicit second-order diffusion term on u with a coefficient of c^2*, analogous to the diffusion term in the Lax-Wendroff scheme.

The numerical scheme can be expressed in the matrix form as

$$\begin{bmatrix} \phi \\ u \end{bmatrix}_j^{n+1} = \begin{bmatrix} \phi \\ u \end{bmatrix}_j^n + \sum_{l=-2N_g}^{2N_g} \begin{bmatrix} 0 & -acA^{(l)} \\ -\frac{c}{a}A^{(l)} & c^2 C_{FB}^{(l)} \end{bmatrix} \begin{bmatrix} \phi \\ u \end{bmatrix}_{j+l}^n \tag{43}$$

Applying the Von Neumann analysis to equation (35) yields the coefficient matrix:
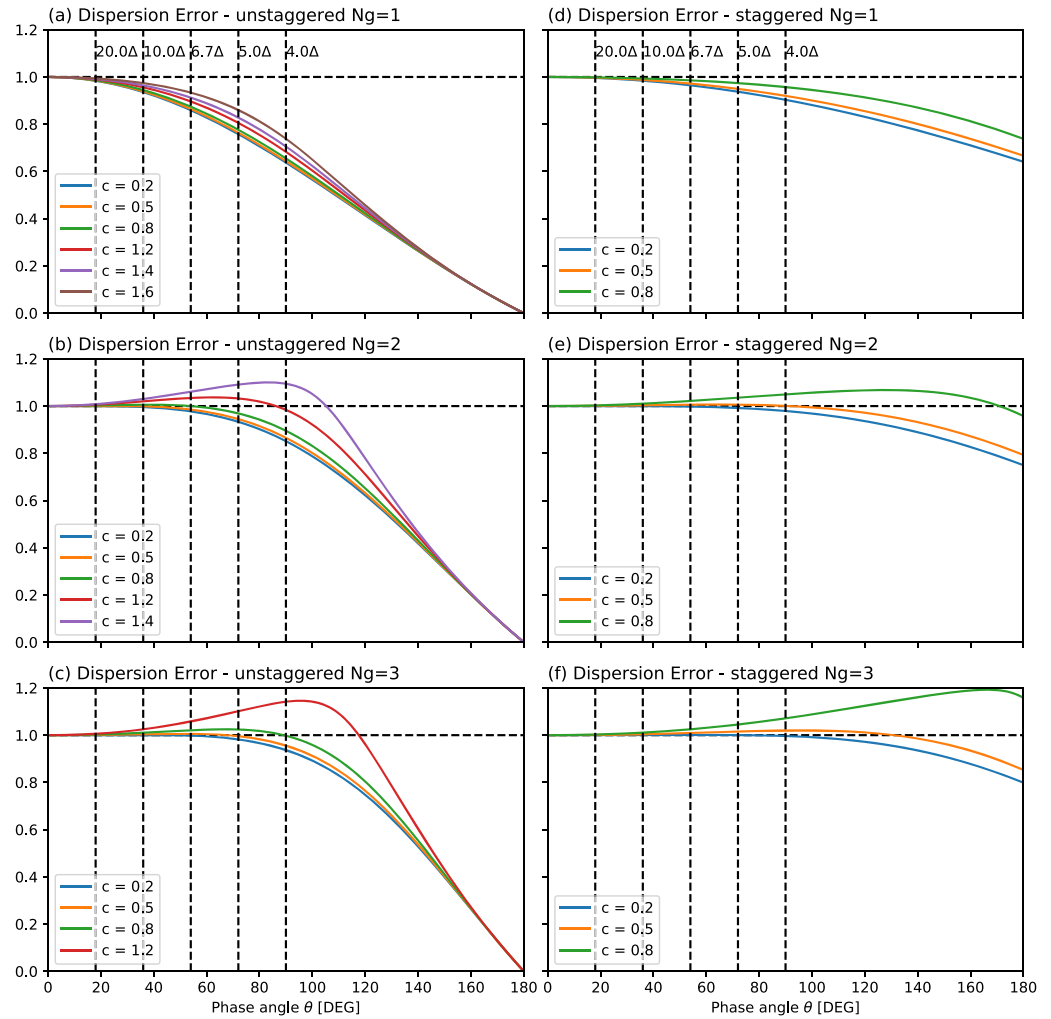
$$P = \begin{bmatrix} 1 & 0 \\ 0 & 1 \end{bmatrix} + \sum_{l=-2N_g}^{2N_g} \begin{bmatrix} 0 & -acA^{(l)} \\ -\frac{c}{a}A^{(l)} & c^2 C_{FB}^{(l)} \end{bmatrix} \exp(il\theta) \tag{44}$$

and the amplification factor G is the eigenvalue to the matrix P.

For $N_g = 1$, the analytical solutions are:

$$G = 1 - \frac{c^2}{2} \sin^2 \theta \pm i\frac{c}{2} \sin \theta \sqrt{4 - c^2 \sin^2 \theta} \tag{45}$$

Figure 3. The dispersion errors of the forward-backward central differencing schemes on both unstaggered grid (left column) and staggered grid (right column) with 3-point stencil ($N_g = 1$, row 1), 5-point stencil ($N_g = 2$, row 2), and 7-point stencil ($N_g = 3$, row 3). The vertical dashed lines are the corresponding phase angles to wave lengths of $4\Delta x$, $5\Delta x$, $6\frac{2}{3}\Delta x$, $10\Delta x$, and $20\Delta x$.

There are two solutions, indicating the wave is propagating to both directions. The largest allowed Courant number is the largest value of c that satisfies $|G| \leq 1$ for all values of θ, and for $N_g = 1$, $c_{max} = 2$. For $|c| \leq 2$, the norm or amplification factor is

$$|G|^2 = \left(1 - \frac{c^2}{2}\sin^2\theta\right)^2 + \left(\frac{c}{2}\sin\theta\sqrt{4 - c^2\sin^2\theta}\right)^2 = 1 \qquad (46)$$

Hence, the dissipative error $\epsilon_v = 1$ and the FB central differencing scheme with unstaggered grid is neutrally stable, which means this scheme has no diffusion error.

The dispersion error can be calculated using equation (37):

$$\epsilon_\phi = \frac{2\sin^{-1}(\frac{c}{2}\sin\theta)}{c\theta} \qquad (47)$$

The dispersion error is dependent on the Courant number c and the phase angle θ. Given the Courant numbers [0.2, 0.5, 0.8, 1.2, 1.4, 1.6], one can plot the dispersion errors as a function of θ in Figure 3a. The dissipation errors are 1 for all values of θ. This scheme allows the Courant number to be greater than 1, an appealing advantage.

Table 3
The Coefficient to Calculate Derivative Value on a Stencil Number of $N_c = 2N_g$ with $A_c^{(l)} = -A_c^{(1-l)}$

N_g	$A_c^{(1)}$	$A_c^{(2)}$	$A_c^{(3)}$
1	1		
2	9/8	−1/24	
3	75/64	−25/384	3/640

3.1.2. Numerical Solution of the Amplification Factor for the High-Order Central Differencing Unstaggered Scheme

Although the coefficient matrix P in equation (44) can be written explicitly, the analytical solutions to the high order schemes are very complicated. Instead of analytical derivation, the eigenvalues G of equation (44) can be evaluated directly using numerical values of c and θ (a is canceled during the calculation of eigenvalues). The numerical-Von-Neumann-analysis-produced solutions to the ϵ_v are 1 for all stable values of c and θ, indicating that high-order FB central-differencing schemes are also inviscid. The dispersion errors are showed in Figures 3b and 3c.

As the spatial order of accuracy of the schemes increases, the maximum stable Courant numbers decreases. In fact, $c_{max} = 1.45$ for $N_g = 2$ and $c_{max} = 1.26$ for $N_g = 3$. All three cases have no dissipation errors since $|G| = 1$. Also, similar to $N_g = 1$ scheme, both high order schemes cannot properly resolve the grid-scale waves, indicated by $\epsilon_v = 0$ when $\theta = \pi$. However, as the order of accuracy increases, the dispersion errors are significantly decreased for other wavelengths if good choice of Courant number is made, for example, $c = 0.8$.

3.2. The Central Differencing Scheme on the Staggered Grid

Again, we define the velocity u_j at the staggered grid location $x_{j-0.5}$ (u is "staggered"). The numerical discretization of staggered schemes can be written as follows:

$$\phi_j^{n+1} = \phi_j^n - ac \sum_{l=-N_g}^{N_g} A_c^{(l)} u_{j+l}^n \tag{48}$$

$$u_j^{n+1} = u_j^n - \frac{c}{a} \sum_{l=-N_g}^{N_g} A_c^{(l)} \phi_{j+l-1}^{n+1} \tag{49}$$

The spatial derivative term will be evaluated by a $N_c = 2N_g$ stencil, satisfying

$$\frac{1}{\Delta x} \sum_{l=1-N_g}^{N_g} A_c^{(l)} \eta_{j+l} = \left. \frac{\partial \eta}{\partial x} \right|_{j+0.5} + O(\Delta x^{2N_g}) \tag{50}$$

The values of coefficient $A_c^{(l)}$ is listed in Table 3.

In the momentum equation (49), the spatial derivative coefficients $A_c^{(l)}$ has a one grid point shift to the variable ϕ. For clarity, an additional utility derivative coefficient is defined as follows:

$$B_c^{(l)} = A_c^{(l+1)} \tag{51}$$

and equation (49) can be rewritten as follows:

$$u_j^{n+1} = u_j^n - \frac{c}{a} \sum_{l=-N_g}^{N_g} B_c^{(l)} \phi_{j+l}^{n+1} =$$

$$u_j^n - \frac{c}{a} \sum_{l=-N_g}^{N_g} B_c^{(l)} \left[\phi_{j+l}^n - ac \sum_{m=-N_g}^{N_g} A_c^{(l)} u_{j+m+l}^n \right] = \tag{52}$$

$$u_j^n - \frac{c}{a} \sum_{l=-N_g}^{N_g} B_c^{(l)} \phi_{j+l}^n + c^2 \sum_{l=-N_g}^{N_g} B_c^{(l)} \sum_{m=-N_g}^{N_g} A_c^{(m)} u_{j+m+l}^n$$

and denote

$$C_{cFB}^{(p)} = \sum_{l=-N_g}^{N_g} B_c^{(l)} A_c^{(p-l)} \tag{53}$$

A Taylor expansion can validate that the $C_{cFB}^{(l)}$ on any variable η satisfies

$$\frac{1}{\Delta x^2} \sum_{l=-2N_g}^{2N_g} C_{cFB}^{(l)} \eta_{j+l} = \left. \frac{\partial^2 \eta}{\partial x^2} \right|_{x_j} + O(\Delta x^{2N_g}) \tag{54}$$

similar to the unstaggered counterpart. Equations (52) and (53) yield

$$u_j^{n+1} = u_j^n - \frac{c}{a} \sum_{l=-N_g}^{N_g} B_c^{(l)} \phi_{j+l}^n + c^2 \sum_{l=-2N_g}^{2N_g} C_{cFB}^{(l)} u_{j+l}^n \tag{55}$$

In matrix form

$$\begin{bmatrix} \phi \\ u \end{bmatrix}_j^{n+1} = \begin{bmatrix} \phi \\ u \end{bmatrix}_j^n + \sum_{l=-2N_g}^{2N_g} \begin{bmatrix} 0 & -acA_c^{(l)} \\ -\frac{c}{a}B_c^{(l)} & c^2 C_{cFB}^{(l)} \end{bmatrix} \begin{bmatrix} \phi \\ u \end{bmatrix}_{j+l}^n \tag{56}$$

Applying the Von Neumann analysis following equation (35) yields the coefficient matrix

$$P = \begin{bmatrix} 1 & 0 \\ 0 & 1 \end{bmatrix} + \sum_{l=-2N_g-1}^{2N_g-1} \begin{bmatrix} 0 & -acA_c^{(l)} \\ -\frac{c}{a}B_c^{(l)} & c^2 C_{cFB}^{(l)} \end{bmatrix} \exp(il\theta) \tag{57}$$

Similar to the unstaggered schemes, G can be evaluated both analytically and numerically. Here the analytical solutions for the lowest order of accuracy are given for reference. For $N_g = 1$,

$$G = 1 - c^2(1 - \cos\theta) \pm ic\sqrt{(1 - \cos\theta)(c^2\cos\theta - c^2 + 2)} \tag{58}$$

Due to the complicated mathematical expression, the high-order analytical solutions are calculated by the numerical Von Neumann analysis. The maximum allowed Courant numbers are $c_{max} = 1$ for $N_g = 1$, $c_{max} = 0.85$ for $N_g = 2$, and $c_{max} = 0.80$ for $N_g = 3$. The numerical solution of the dispersion properties e_ϕ for all stable values of c and θ and dispersion errors are shown in Figures 3d, 3e, and 3f. It is also observed that all staggered schemes have no dissipation errors since $|G| = 1$ or $\epsilon_v = 1$, and thus are inviscid.

Comparing the schemes on staggered and unstaggered grids, both schemes at all orders of accuracy have no dissipation errors, which will maintain the amplitude of the solution at all wave numbers perfectly. However, neutrally stable schemes have some unfavorable consequences because *high-frequency errors will not be damped, especially for the grid-size noise at the wavelength of $2\Delta x$*. It is challenging for a central differencing scheme to maintain clean and stable solutions without adding additional explicit diffusion in a real-world application.

Comparing the low-order methods ($N_g = 1$), the staggered grid schemes have obvious advantages over unstaggered grid schemes resolving short waves. However, the unstaggered schemes allow greater time steps than the staggered grid schemes. *The difference in dispersion errors and maximum allowed Courant number, due to grid staggering choices significantly diminish with higher order schemes.*

Even though the two-delta waves have smaller dispersion errors in a staggered grid scheme, the errors accumulate in each integration. After n times integration, the dispersion error will be ϵ_ϕ^n, and these waves will be "out of phase" rapidly. As a result, waves at the shortest scale cannot be trusted in both staggered and unstaggered grid and should be removed by numerical filters. This issue will be further discussed in the following section.

3.3. The Unstaggered Scheme With the Riemann Solver
The main benefit from a Riemann solver is the better treatment to nonlinearities in numerical solutions. Pairing the Riemann solvers with a monotonic subgrid reconstruction provides suitable implicit diffusion to nonlinear

processes, such as discontinuities, without creating overshoots and undershoots. The mathematical expression of the implicit diffusion will be derived in this subsection. Instead of using equation (19), the volume interface values will be calculated using the LMARS from equations (14) and (15). The mismatched local cell boundary values are

$$u_j^E = \sum_{l=-N_g}^{N_g} E^{(l)} u_{j+l} \tag{59}$$

$$u_j^W = \sum_{l=-N_g}^{N_g} W^{(l)} u_{j+l} \tag{60}$$

$$\phi_j^E = \sum_{l=-N_g}^{N_g} E^{(l)} \phi_{j+l} \tag{61}$$

$$\phi_j^W = \sum_{l=-N_g}^{N_g} W^{(l)} \phi_{j+l} \tag{62}$$

The cell interface values are

$$u_{j+0.5} = \frac{1}{2}(u_j^E + u_{j+1}^W) + \frac{1}{2a}(\phi_j^E - \phi_{j+1}^W) \tag{63}$$

$$\phi_{j+0.5} = \frac{1}{2}(\phi_j^E + \phi_{j+1}^W) + \frac{a}{2}(u_j^E - u_{j+1}^W) \tag{64}$$

or

$$u_{j+0.5} = \sum_l M^{(l)} u_{j+l} + \frac{1}{a} \sum_l D^{(l)} \phi_{j+l} \tag{65}$$

$$\phi_{j+0.5} = \sum_l M^{(l)} \phi_{j+l} + a \sum_l D^{(l)} u_{j+l} \tag{66}$$

where

$$D^{(l)} = \frac{1}{2}(E^{(l)} - W^{(l-1)}) \tag{67}$$

The coefficients $D^{(l)}$ result from the variable mismatches at the volume interfaces. This work assumes the volume-mean variables, and we write $D^{(l)} = D_{vm}^{(l)}$ for simplicity.

The numerical discretization using LMARS can be written as follows:

$$\phi_j^{n+1} = \phi_j^n - ac \left(u_{j+0.5}^n - u_{j-0.5}^n \right) \tag{68}$$

$$u_j^{n+1} = u_j^n - \frac{c}{a} \left(\phi_{j+0.5}^{n+1} - \phi_{j-0.5}^{n+1} \right) \tag{69}$$

Replacing the interface values with equations (65) and (66):

$$\phi_j^{n+1} = \phi_j^n - ac \sum_l A^{(l)} u_{j+l}^n + c \sum_l C_{vmRS}^{(l)} \phi_{j+l}^n \tag{70}$$

$$u_j^{n+1} = u_j^n - \frac{c}{a} \sum_l A^{(l)} \phi_{j+l}^{n+1} + c \sum_l C_{vmRS}^{(l)} u_{j+l}^n \tag{71}$$

where the $C_{vmRS}^{(l)}$ denotes the diffusion terms that are introduced by the Riemann solver with
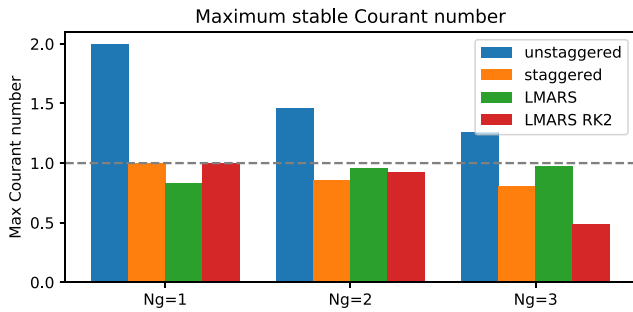
$$C_{vmRS}^{(l)} = -D_{vm}^{(l)} + D_{vm}^{(l+1)} \tag{72}$$

A Taylor expansion shows that the $C_{vmRS}^{(l)}$ on any variable η satisfies

$$\frac{1}{\Delta x^{2N_g}} \sum_l C_{vmRS}^{(l)} \eta_{j+l} = \nu \frac{\partial^{2N_g} \eta}{\partial x^{2N_g}} \bigg|_{x_j} + O(\Delta x^2) \tag{73}$$

where

$$\nu = \begin{cases} \frac{1}{2} & N_g = 1 \\ -\frac{1}{12} & N_g = 2 \\ \frac{1}{60} & N_g = 3 \end{cases} \tag{74}$$

Figure 4. The maximum allowed Courant numbers for four numerical discretization in three different order of accuracies.

Thus, *the LMARS automatically provides the matched high-order diffusion term to both prognostic variables based on the interpolation order of accuracy*. The implicit diffusion does not require significant additional computing steps, which is beneficial to the dynamical core's efficiency. If monotone and nonoscillatory properties are desired, the monotonic limiter or ENO/WENO schemes can be implemented following the standard procedures described in van Leer (1974, 1979), Colella and Woodward (1984), and Shu and Osher (1988), and the local nonlinear adjustment is applied to the LMARS algorithm. These nonlinear schemes are beyond the scope of this analysis.

A special adjustment is made in equation (71): the diffusion term is at time-step n instead of $n + 1$. With this numerical adjustment, the Riemann solver would only act once on ϕ, which enhances the efficiency of this algorithm. If LMARS needs to be evaluated twice, a two-step Runge-Kutta method (RK2) is one of the more standard choices at this cost. The analysis of the LMARS RK2 algorithm is described in Appendix A. However, it is not found that RK2 is significantly better than the optimized FB method, especially the CFL condition is more severely constrained in $N_g = 3$ case.

The analytical solutions for the amplification factor G can be complicated. Instead, numerical Von Neumann analysis is applied to analyze the implicit discretization. In practice, the sum operation of $\sum_l$ can be simply extended to a large value, i.e., $\sum_{l=-20}^{20}$ with zero values when the coefficients are out of the computational stencil. Equations (70) and 71 can be rewritten as follows:

$$L \begin{bmatrix} \phi \\ u \end{bmatrix}_{j+l}^{n+1} = R \begin{bmatrix} \phi \\ u \end{bmatrix}_{j+l}^{n} \tag{75}$$

where

$$L = \begin{bmatrix} 1 & 0 \\ 0 & 1 \end{bmatrix} + \sum_l \begin{bmatrix} 0 & 0 \\ \frac{c}{a} A^{(l)} & 0 \end{bmatrix} \exp(il\theta) \tag{76}$$

$$R = \begin{bmatrix} 1 & 0 \\ 0 & 1 \end{bmatrix} + \sum_l \begin{bmatrix} cC_{vmRS}^{(l)} & -acA^{(l)} \\ 0 & cC_{vmRS}^{(l)} \end{bmatrix} \exp(il\theta) \tag{77}$$

The inverse of L is

$$L^{-1} = \begin{bmatrix} 1 & 0 \\ 0 & 1 \end{bmatrix} + \sum_l \begin{bmatrix} 0 & 0 \\ -\frac{c}{a} A^{(l)} & 0 \end{bmatrix} \exp(il\theta) \tag{78}$$

From the Von Neumann analysis, the amplification factor G satisfies equation (35) where

$$P = L^{-1}R \tag{79}$$

The maximum allowed Courant numbers are $c_{max} = 0.83$ for $N_g = 1$; $c_{max} = 0.96$ for $N_g = 2$; and $c_{max} = 0.97$ for $N_g = 3$. Figure 4 illustrates the maximum allowed CFL numbers for all three numerical discretizations discussed in the main text and the LMARS RK2 scheme in the appendix in three different orders of accuracy. The numerical estimation of the dissipation and dispersion errors are shown in Figure 5. Unlike the unstaggered central differencing scheme, the dispersion of two-delta waves are no longer stationary with LMARS. As demonstrated in this section, the LMARS approach can be alternatively considered as an unstaggered discretization with a high-order numerical diffusion. Therefore, it indicates that *the diffusion scheme can have a significant impact on the dispersion properties of a numerical scheme*. This is an example of an unstaggered numerical scheme that does not have stationary signals of grid-scale wavelength. Another finding is that for low-order cases ($N_g = 1$), the dissipation error is so large that even the signals with 20 times grid length are likely to be damped out completely. Thus the low-order Riemann solver schemes are not practical.

Admittedly, the analytical solutions of the dispersive relation to the Von Neumann analysis has unique merits. Staniforth et al. (2013) use it to guide the numerical modification to solve the "spectral gap" problem. However, even with the almost lowest possible order modified mixed-element scheme, the mathematical expression for the amplification factor is already complicated in Staniforth et al. (2013). Modern software such as Maple or
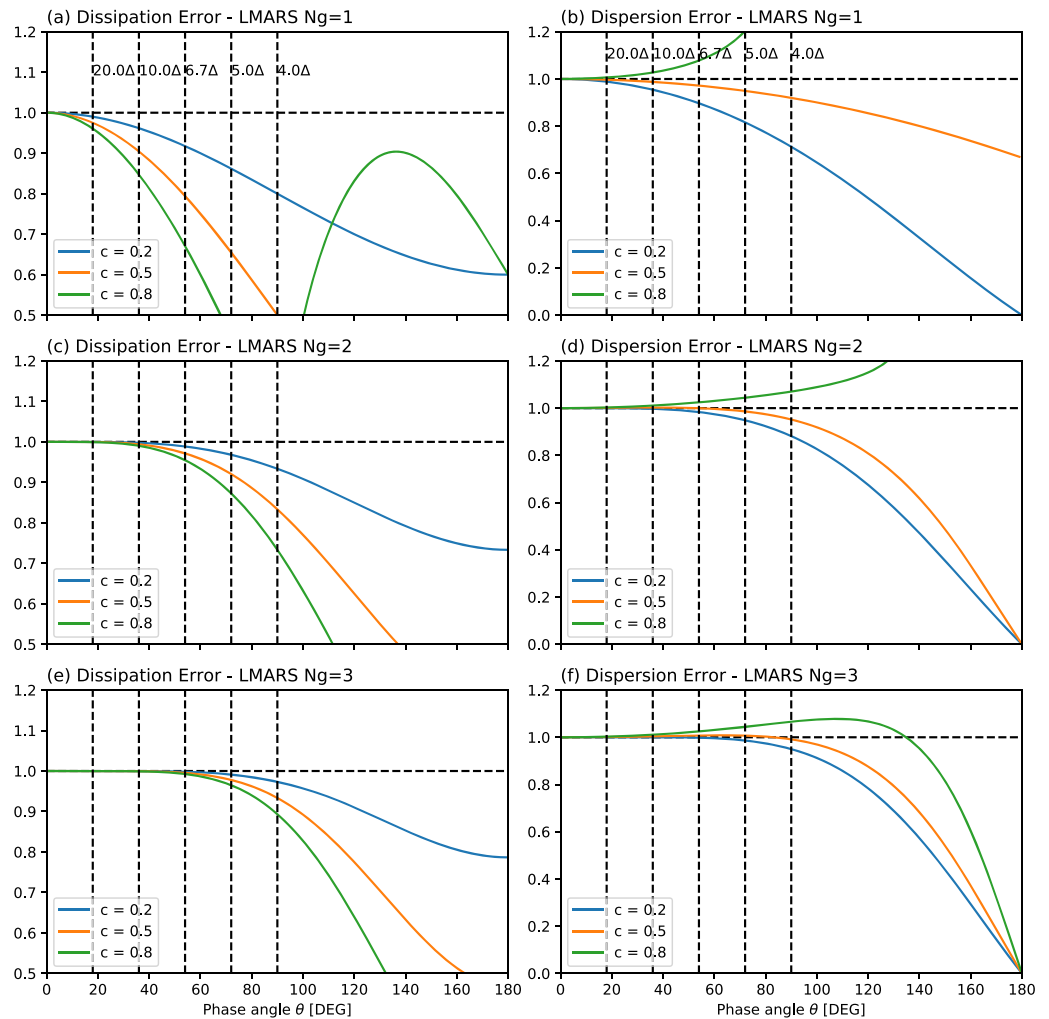
Figure 5. The dissipation (left column) and dispersion (right column) errors of the forward-backward Riemann-solver schemes with 3-point stencil ($N_g = 1$, row 1), 5-point stencil ($N_g = 2$, row 2), and 7-point stencil ($N_g = 3$, row 3). The vertical dashed lines are the corresponding phase angles to wave lengths of $4\Delta x$, $5\Delta x$, $6\frac{2}{3}\Delta x$, $10\Delta x$, and $20\Delta x$.

Mathematica have packages for algebraic calculation, but even with the help of these packages, solving the high-order schemes could result in calculation out of the computer precision limit, and the algebraic solutions could be unphysical (Eldred & Le Roux, 2018). Therefore, using discrete values of c and θ to calculate the dispersion relation numerically is a useful tool to understand the numerical properties of complicated high-order schemes. The two-step Runge-Kutta LMARS linear analysis conducted in Appendix A is another example of even more complicated multistep numerical discretization implementation of this "numerical" Von Neumann approach.

4. Numerical Experiments

As illustrated in the previous section, the diffusion scheme can significantly alter the dispersion properties. Since all modern dynamical cores implement multiple types of diffusive terms and filters, it is difficult to perform the Von Neumann analysis on each set of the diffusion parameters to understand the dispersion properties. More importantly, how the combined effects of dispersion and dissipation affect a more realistic simulation is not explicit, especially when steep gradients arise. Therefore, a suite of tests is designed to evaluate the interaction between the dissipation and dispersion at specific wave numbers. The tests also reveal the robustness of the schemes when encountering discontinuities. As is conventional, the flow height $h = \phi/g$ is used as the prognostic variable.

4.1. Test Case Design

The tests are formulated within a one-dimensional computational domain. We choose H so that the group or the gravity wave speed is $a = \sqrt{gH} = 10$ m/s. Since the gravitational acceleration g is trivial in our discussion, it will be normalized to $g = 10$ m/s^2 to make values of H integers. The perturbation amplitude of the flow height is $h_0 = 1$ m. The grid spacing is set to $\Delta x = 100$ m so that each kilometer contains $N = 10$ grid points. The tests are simple to setup: Two symmetric waves with identical wave numbers but opposite propagating directions are defined

$$h_1 = h_0 \sin(kx - akt) \tag{80}$$

$$u_1 = \sqrt{g/H}h_0 \sin(kx - akt) \tag{81}$$

$$h_2 = h_0 \sin(kx + akt) \tag{82}$$

$$u_2 = -\sqrt{g/H}h_0 \sin(kx + akt) \tag{83}$$

and are initialized in the range $-1{,}000 \leq x \leq 1{,}000$ m. The initial condition of the flow is the sum of the two waves:

$$h = h_1 + h_2 \tag{84}$$

$$u = u_1 + u_2 \tag{85}$$

which results in a zero-velocity field.

The computational domain is expanded to $x = [-10000, 10000]$ m, with zero initial perturbation outside of the $[-1000, 1000]$ m range.

The test cases implemented in Staniforth et al. (2013) are similar in many ways. However, a significant difference is, in their setup, the periodic high-frequency field is enveloped by a Gaussian profile, resulting in a continuous flow field everywhere within the domain. To better evaluate behavior near discontinuities and keep only single frequency in the simulation, the signal is modulated by a square wave instead of the smooth Gaussian profile used in Staniforth et al. (2013).

The longest resolvable wave contains 20 grid points, which should be considered sufficient to be resolved properly in most high-order numerical schemes. The shortest resolvable wavelength is $2\Delta x = 200$ m. The corresponding phase angle to each wave number (in degrees) is given by

$$\theta_{deg} = k_m \Delta x = \frac{180m}{N} = 18m, \quad m = 1, \ldots, 10 \tag{86}$$

A special case with $m = 0$ yields square wave profiles of the height perturbation and velocity field:

$$h_1 = h_0 \tag{87}$$

$$u_1 = \sqrt{g/H}h_0 \tag{88}$$

$$h_2 = h_0 \tag{89}$$

$$u_2 = -\sqrt{g/H}h_0 \tag{90}$$

This is a special case that is useful for observing how the numerical scheme handles strong gradients and how the numerical errors propagate in the simulation.

The total integration time is set to $T_{tot} = 800$ s. In the linearized shallow water system, the two original waves will theoretically propagate following two characteristic lines: $x \pm at = 0$. Thus at the end of the simulation, the two waves should be cleanly separated and propagate to $x = [-9000, -7000]$ m, and $x = [7000, 9000]$ m. The perturbation field is indicated by wave height, defined by $h - H$. Although unstaggered numerical schemes allow Courant number larger than 1, to compare results under identical Courant number, the time step is set to be $\Delta t = 8$ s for all cases, or $c = 0.8$.
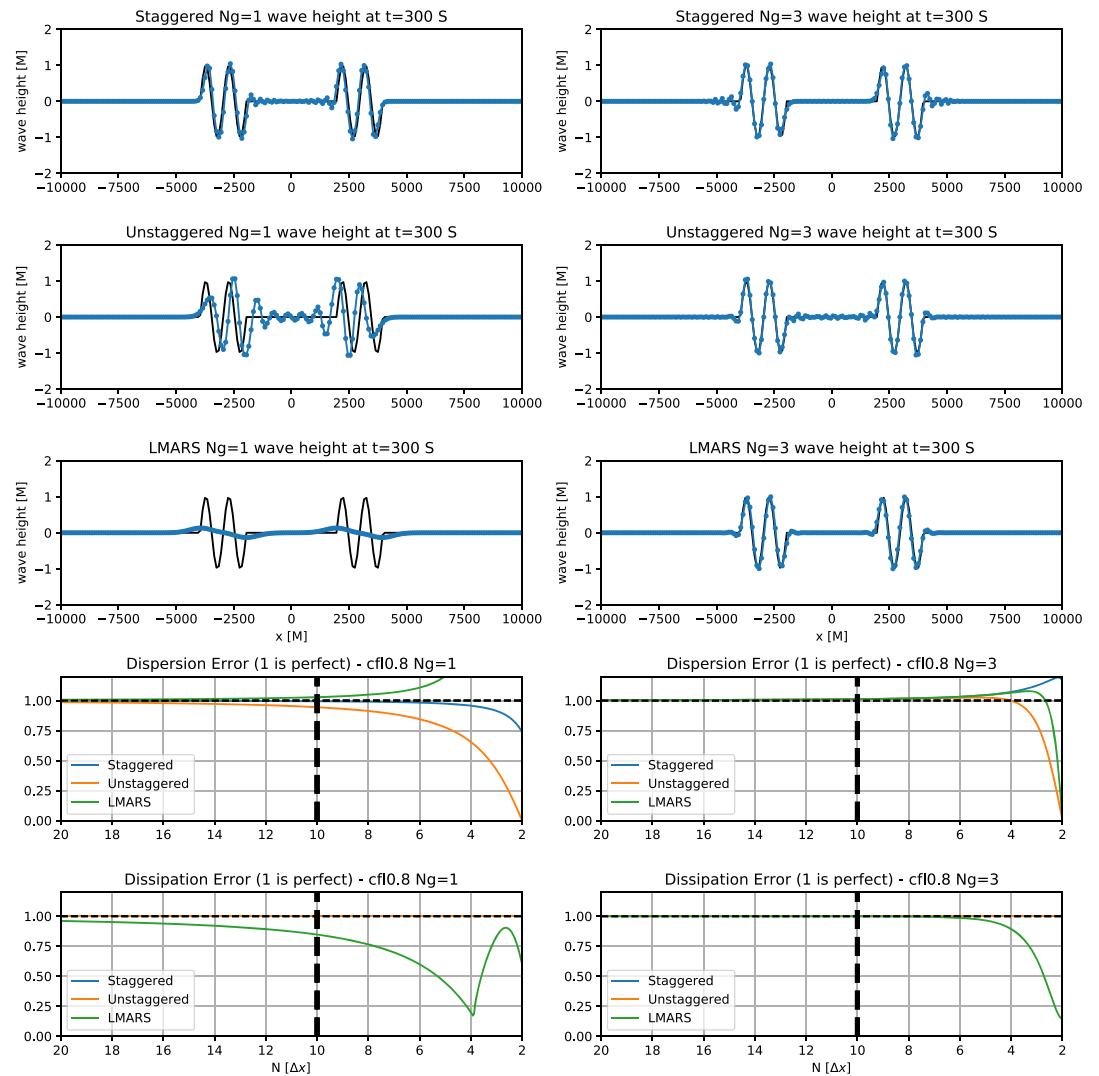
Figure 6. The 10-delta-wave tests using low-order $N_g = 1$ schemes (left) and high-order $N_g = 3$ schemes (right). The first three rows are the wave height ($h - H$) of the staggered, unstaggered and LMARS schemes at $t = 300$ s, respectively. The last two rows are the dispersion and dissipation relations of respective methods at different orders of accuracy. Note that these two plots are reorganizations of Figures 3 and 5, with the horizontal axis replaced by the wavelength in the unit of grid spacing. The black vertical dashed line corresponds to the values of phase and diffusion errors at 10-delta wavelength.

4.2. The 10-Delta-Wave Tests

The first test is conducted using $m = 2$, or wavelength $10\Delta x$. For brevity, the tests compare the numerical schemes using the shortest computational stencil of 3 points or $N_g = 1$ and longest computational stencil of 7 points or $N_g = 3$.

Figure 6 shows the 10-delta-wave tests using low-order $N_g = 1$ schemes and high-order $N_g = 3$ schemes. The first three rows are the wave height ($h - H$) of the staggered, unstaggered and LMARS schemes at $t = 300$ s, respectively. The solid black lines are the reference solutions given by equation (84). The last two rows are the dispersion and dissipation relations of respective methods at different orders of accuracy. Note that these two plots are reorganizations of Figures 3 and 5, with the horizontal axis replaced by the wavelength in the unit of grid spacing. The thick black vertical dashed line is corresponding to the values of phase and diffusion errors at 10-delta-wavelength. The two branches of waves cleanly separate at $t = 300$ s. Although at the end of the run ($t = 800$ s), both waves are still within the computational domain, some of the fast propagating waves with $e_\phi > 1$, could travel through the boundaries and compound with the signals on the other branch, thus contaminating the error analysis. Therefore, all snapshots of the wave height solution are taken at $t = 300$ s.
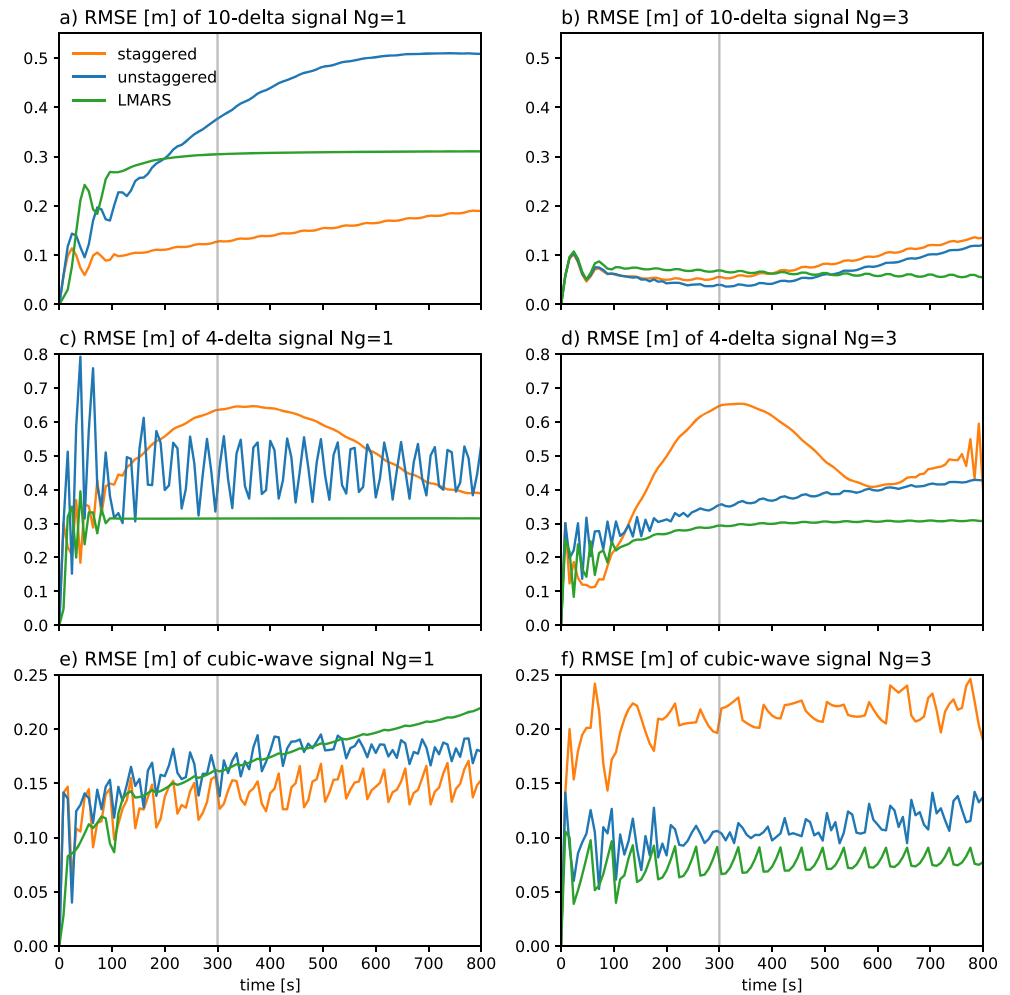
Figure 7. The growth of the root-mean-square error (RMSE) in time of different schemes at different wavelengths. The left column is the RMSE growth of low-order ($N_g = 1$) schemes; the right column is the RMSE growth of high-order ($N_g = 3$) schemes. The first row is the analysis of 10-delta-wave simulations. The second row is the analysis of four-delta-wave simulations. The third row is the analysis of the "square"-wave simulations. The gray lines indicate the simulation time $t = 300$ s of the snapshots of the wave height plots.

It can be observed that even for a long wave with 10 grid points to resolve it, the low-order unstaggered scheme still has a slight phase lag. The lag is consistent with the theoretical analysis that the unstaggered solution has a noticeable slower group speed than staggered solution at wavelength $10\Delta x$, while the staggered scheme almost perfectly maintains the phase speed compared to the reference solutions. Because the dissipative effect of the LMARS $N_g = 1$ case is still strong at $10\Delta x$, it can be observed the long waves are almost completely damped and making the problematic too-fast dispersion error property trivial. Since 10-delta-waves are expected to be "well-resolved," low-order LMARS schemes should be considered too dissipative for practical applications.

All three schemes perform well with high-order $N_g = 3$ accuracy. It is safe to claim that the 10-delta waves can be well resolved in all three schemes. Note that both inviscid schemes introduce noise due to discontinuities. The LMARS scheme shows better control of the noise.

The root-mean-square error (RMSE) is defined with respect to the analytical solutions. With any stable scheme for this numerical test, the RMSE should plateau after a certain period, when: a) the solutions are entirely out-of-phase, or b) the solutions are completely diffused. At 10-delta wavelength, the dispersion errors are relatively small, and the three numerical solutions will not be out-of-phase. Therefore, the RMSE analysis is an objective perspective to judge the performance of the numerical solutions in this tests.
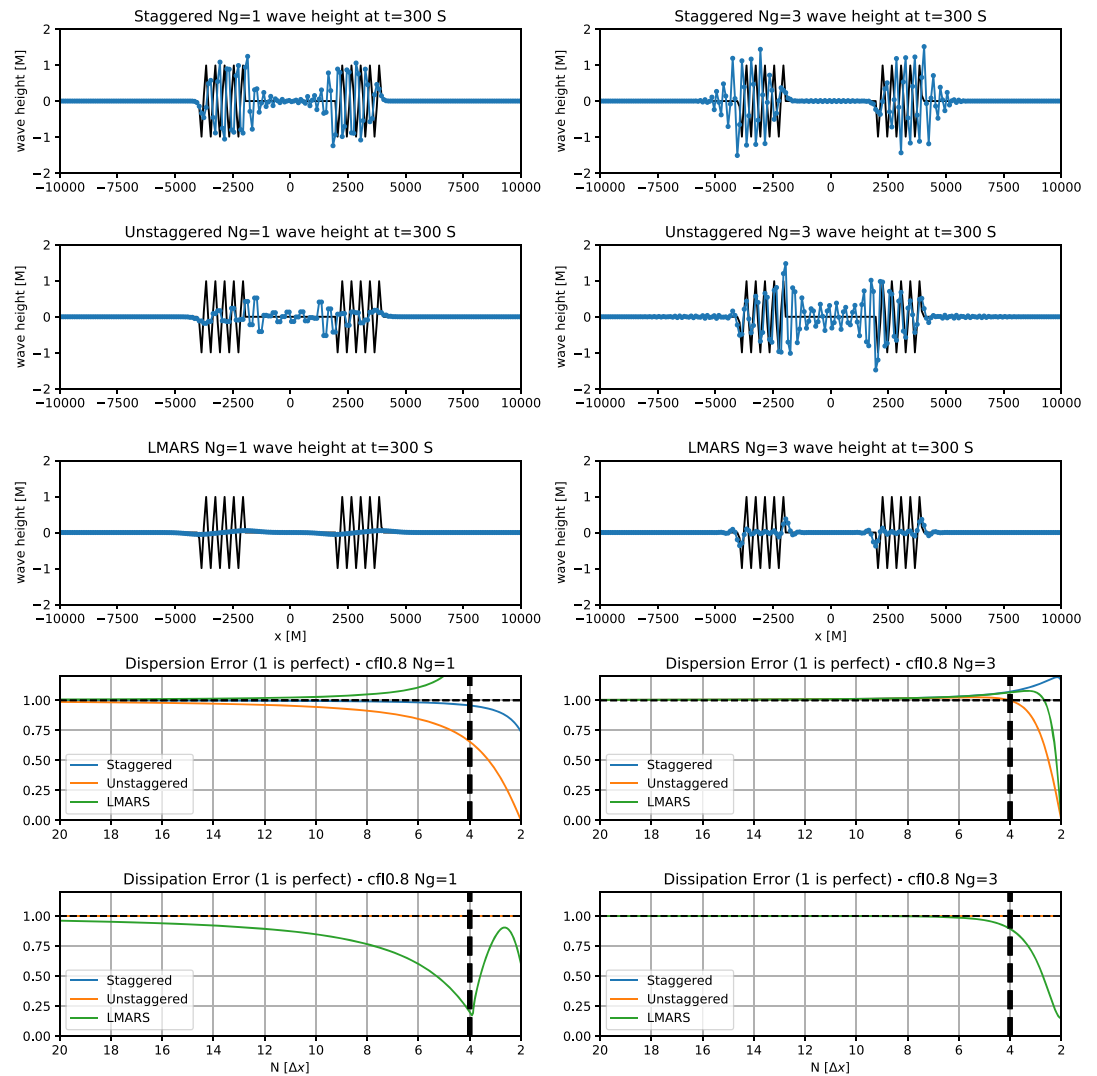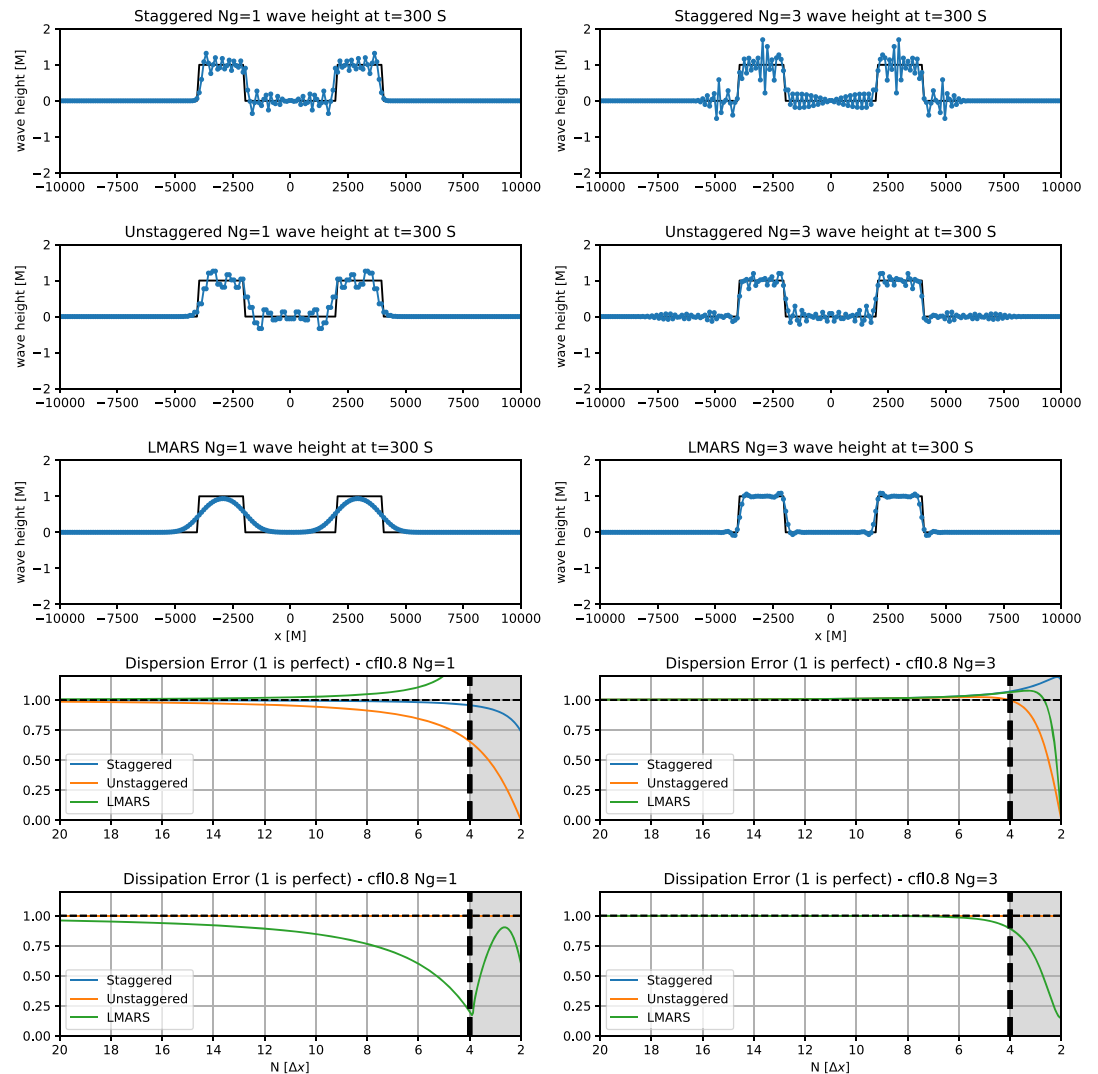
Figure 8. Same as Figure 6 except the simulations are of four-delta wavelength. The red dashed lines indicate the dispersive and dissipative properties at the corresponding four-delta wavelength.

Figure 7a and b demonstrate the growth of the RMSE for different schemes at 10-delta wavelength ($m = 2$). The left panel is the RMSE growth of low-order ($N_g = 1$) schemes; the right panel is the RMSE growth of the high-order ($N_g = 3$) schemes. The two branches of the waves complete the separation after approximately 100 s. Within the first 100 s, the amplitudes of the reference solution change periodically, and the change in amplitudes of the RMSE is correlated. After the separation, the two reference branches is essentially constant transportation. Therefore, if RMSE oscillates after the completion of the wave separation (100 s), it is due to the high-frequency numerical noise caused by the discontinuities.

In the low-order simulations, the staggered scheme has the best representation of the 10-delta waves with the lowest errors. Interestingly, the LMARS errors stop growing after approximately 200 seconds, which is not necessarily encouraging because by observing the simulation, the 10-delta waves are almost entirely dissipated. The superior performance at 10-delta wavelength of the inviscid low-order staggered scheme comes from the better dispersion properties, which is in agreement with most traditional analysis and perceptions.

In high-order runs, however, the conclusions from the low-order runs are almost reversed. All three high-order schemes have minimum dispersive and dissipative errors, and the primary 10-delta signals are adequately maintained, as proved by the small absolute magnitude of the RMSE values. From Figure 6 it can be observed that both inviscid schemes - staggered or unstaggered - introduce weak high-frequency noise at the discon-

Figure 9. Same as Figure 6 except the simulations propagate square wave signals. The gray shaded regions in the bottom two rows indicate the dispersive and dissipative properties of the numerical noise introduced by the discontinuities.

tinuities between the primary signals and the background. Without proper diffusion, the noise accumulates in time as observed in Figure 7b. The RMSE of LMARS scheme does not grow owing to the effective high-frequency noise removal.

4.3. The Four-Delta-Wave Tests

Figure 8 is the same as Figure 6 except the simulations are of four-delta wavelength or $m = 5$. The black dashed lines indicate the dispersive and dissipative properties at the corresponding four-delta wavelength.

The low-order unstaggered scheme is inviscid. However, due to the enormous dispersive errors, all high-frequency signals - real solutions or noise - are stationary. The low-order staggered scheme has better dispersive properties, and the high-frequency signals follow the reference solutions more closely than the staggered results. However, the phase error is still significant, and as the simulation progresses, the solutions will be out-of-phase quickly. Both staggered and unstaggered inviscid schemes introduce high-frequency noise between the two branches of the waves due to the discontinuities. Similar to previous long-wave tests, because the dissipative effect of the low-order $N_g = 1$ LMARS scheme is dominant at $4\Delta x$, the problematic too-fast dispersion error property is insignificant since all information is dissipated entirely.

In the high-order short-wave simulations, judged by the analytical dispersive errors in row 4 of Figure 8, the unstaggered scheme should - in fact, contrary to the traditional perspective - have the best dispersion

properties among all three solutions. Indeed, the high-order unstaggered numerical solution matches the phase speed of the reference solution almost perfectly at $t = 300$ s. The short-wave signals of the staggered numerical solutions are slightly faster than the reference solutions, which matches the theoretical conclusion suggested in row 4 of Figure 8. Although the inviscid unstaggered scheme has good dispersion properties, can the solution be considered desirable for this test? Not exactly. The noise due to discontinuities is distributed between two moving branches of the signals, which has the comparable magnitude of the actual signals. Visually, if the reference solution is ignored, the unstaggered wave pattern looks like two connected giant energy packages growing in both directions, which is unrealistic compared to the reference. Therefore, even with the almost perfect dispersion properties, the inviscid unstaggered scheme resolves four-delta waves poorly due to the lack of proper mechanism to suppress the nonlinear noise caused by the discontinuities. In the high-order LMARS run, due to the strong dissipation curve at four-delta, all signals are dissipated. The residuals are due to the discontinuities. Therefore, in the high-order LMARS scheme, the four-delta signals are not only "unresolvable" but also entirely removed.

The error growth for the four-delta wave tests (Figure 7c,d) is greatest for the staggered inviscid scheme, regardless of the order of accuracy, due to the substantial generation of undamped grid-scale noise. Further, the higher order staggered scheme begins to show substantial phase error, thereby increasing the RMSE further. The phasing of the numerical and exact solutions changes with time, resulting in a low-frequency oscillation in the error. The low-order unstaggered solution has substantial dispersion error and the slow numerical solution is quickly out of phase with the exact solution, creating large RMSE. However, at higher order the phase error is greatly improved, and in fact has lower phase errors than the high-order staggered scheme, so the RMSE is nearly always smaller. This is contrary to the broad perception that staggered schemes are superior to unstaggered schemes for short-wavelength modes, which is based entirely on the behavior of low-order methods.

It is notable that LMARS has the smallest RMSE for all orders of accuracy, although this is due to the diffusive properties of LMARS, which quickly eliminates the four-delta signal. While the signal is damped, there is also no generation of grid-scale noise.

4.4. The Square Wave Tests

In this subsection, the numerical schemes undergo a more "stressful" test using a zero-wave-number condition. In this test, all the generated short waves from the numerical solvers are noise. This test uses the special wave number $m = 0$, yielding square waves in both directions.

Figure 9 is the same as Figure 6 except the simulations propagate square signals. The gray shaded regions in the bottom two rows indicate the corresponding dispersive and dissipative properties of the numerical noise introduced by the discontinuities.

In the low-order simulations, both staggered and unstaggered results show significant two-delta to four-delta noise which is produced by the discontinuities. Suggested by the shaded regions of the dispersion curves, noise in both inviscid simulations should be stationary after multiple time integrations. Indeed, as shown in both inviscid simulations, the high-frequency noise distributes relatively evenly in the upwind region between the two square signals. The amplitude of the noise is comparable between different staggering choices. The Riemann solver solutions, on the other hand, are diffusive due to the drastic dissipation effect at short wavelengths, and again, the dispersion properties of LMARS is irrelevant in this test. Arguably, all three schemes perform poorly with low-order discretization in this square wave tests.

The high-order simulations, on the other hand, are much more interesting. The noise of the high-order unstaggered scheme is relatively evenly distributed in both upwind and downwind regions. However, suggested by the dispersion curve of the staggered scheme, $e_\phi > 1$ at grid-scale wavelengths, the noise should travel faster than the reference wave speed in both positive and negative directions. Such behavior causes a compounding effect that the earlier generated noise can interact with later generated noise and significant low-frequency aliasing can be observed. The low-frequency aliasing can be considered low-frequency energy wave packets, which is difficult to remove by the numerical filters. Similar low-frequency aliasing scenarios caused by the high-order staggered schemes were also reported in Harris and Durran (2010), and Ullrich and Jablonowski (2011), in which the numerical noise is triggered by sudden discontinuities between non-uniform grid spacing regions. For the LMARS scheme, the dissipation curve indicates high-order LMARS scheme can efficiently damp the short wavelength signals below the wavelength of $6\Delta x$. Thus, most high wave number noise caused

by the discontinuities is effectively removed. A desirable solution is observed although there are still over-shoots and undershoots near the discontinuities. The residual overshoot and undershoot noise could be addressed by other numerical techniques such as the monotonic limiters of Lin (2004).

Although all three low-order schemes perform poorly in this test (Figure 7e), the magnitudes of the RMSE are comparable between three simulations. The staggered RMSE is the smallest indicates that the low-order inviscid staggered scheme can be considered "less wrong" in the discontinuous environment.

In high-order simulations (Figure 7f), although the sharpness of the discontinuities is the strongest among all three tests ($m = 2, 5,$ and 0), the magnitude of the noise or RMSE is not the worst. Judged by both wave patterns and the absolute RMSE values, the high-order LMARS scheme performs best in this highly nonlinear environment, thanks to the implicit scale-selective diffusion on the high-frequency waves. The high-order staggered RMSE is almost twice as large than the other two schemes, which is caused by the larger amplitude of the low-frequency aliasing.

4.5. Summary of the Idealized Tests

Although these tests are relatively easy to construct, many numerical properties of three numerical schemes are revealed. The simulation results are consistent with the theoretical Von Neumann analysis. The calculation of the RMSEs for each simulation provides an alternative perspective to gauge the dispersion properties in a quantitive way. Theoretically, the tests introduced in this work should be easy to extend to the 2-D double-periodic environment. Therefore, future LMARS development can reuse this test for validating dispersion properties.

5. Conclusions and Discussion

Several practical methods—both theoretical and numerical solutions—are demonstrated to get the dispersion and dissipation properties of numerical discretization schemes with different orders of accuracy with respect to the Courant number and numerical phase. Analyzing the properties of high-order schemes provides alternative perspectives to many conclusions which are acquired from traditional low-order Von Neumann analysis.

Traditionally, unstaggered schemes are considered problematic near the grid-scale, due to poor dispersive properties revealed by low-order von Neumann or other linearized analysis. However, the linear dispersion properties of sophisticated high-order algorithms are not well understood or well appreciated due to the potentially massive algebraic calculations. The FB scheme is employed to create the "simplest-possible" staggered and unstaggered discretizations for dispersion analysis of the high-order schemes. It is found that the differences due to grid staggering choices are diminishing with higher-order discretization. This work begins the development of a full-featured unstaggered solver for high-resolution geophysical fluid applications by understanding LMARS-based unstaggered solver's dispersion properties. It is also found that the concerns of poor dispersion properties near the grid-scale are manageable for the unstaggered LMARS framework.

Many current high-resolution (≤ 25 km) geophysical fluid simulations need to consider substantial temperature or wind gradients. As illustrated by wave number-zero tests using inviscid schemes - either staggered or unstaggered - the amplitude of the error increases continuously, and the solution is destroyed after a short time of integration. The discontinuities generate strong short-wave oscillations without being damped. Due to these reasons, in high-resolution geophysical fluid applications which might encounter nonlinear solutions, the numerical diffusion—either linear, such as hyper-viscosity, divergence/vorticity damping; or nonlinear, such as monotonic limiter or ENO/WENO schemes—is essential.

Judged by the theoretical dispersion and dissipation error curves in Figures 6, 8, and 9, the staggered schemes appear to have much better dispersion properties at the two-delta wavelength than the unstaggered grid. However, if the grid-scale noise is considered not distinguishable from the real information and the two-delta waves get steadily dissipated, dispersion properties at this scale become irrelevant. Therefore,

Poor dispersion properties at grid-scale are not problematic as long as numerical dissipation selectively removes such waves.

Ideally, considering nonlinear requirements of the numerical schemes, the "right" amount of dissipation should result in that the smallest resolvable wavelength due to the diffusive limit matches the smallest resolvable wavelength due to the dispersive limit. An overdiffused scheme might sacrifice too much meaningful

information, and an under-diffused scheme might generate too much numerical noise due to discontinuities. In this work, the dissipation error curve of the LMARS schemes nicely matches the dispersion error curves, as observed in Figure 5. From the practical perspective (Figure 6), the high-order Riemann solver-based scheme shows very little dissipation when simulating 10-delta waves, demonstrating optimum performance in well-resolved scales. With strong shortwave (two-delta to six-delta) diffusion, the noise due to discontinuity is minimized. Therefore, high-order LMARS schemes are the ideal foundation for future exploration.

Although the 1-D idealized tests introduced in this work focus on the interaction of the dispersion and dissipation, the 2-D tests in a doubly periodic domain or even on the sphere could be easily constructed analogously. The 2-D case can reveal other essential properties, such as the wave propagation speed variation to azimuth angles, or the kinetic energy dissipation rate. The 2-D tests will be introduced in the next installment of LMARS applications on the cubed-sphere geometry.

Appendix A: Analysis of Two-Step Runge-Kutta LMARS Algorithm

The two-step Runge-Kutta scheme with the LMARS algorithm can be discretized in the following form:

$$\phi_j^* = \phi_j^n - \frac{1}{2} a c \sum_l A^{(l)} u_{j+l}^n + \frac{1}{2} c \sum_l C_{vmRS}^{(l)} \phi_{j+l}^n \tag{A1}$$
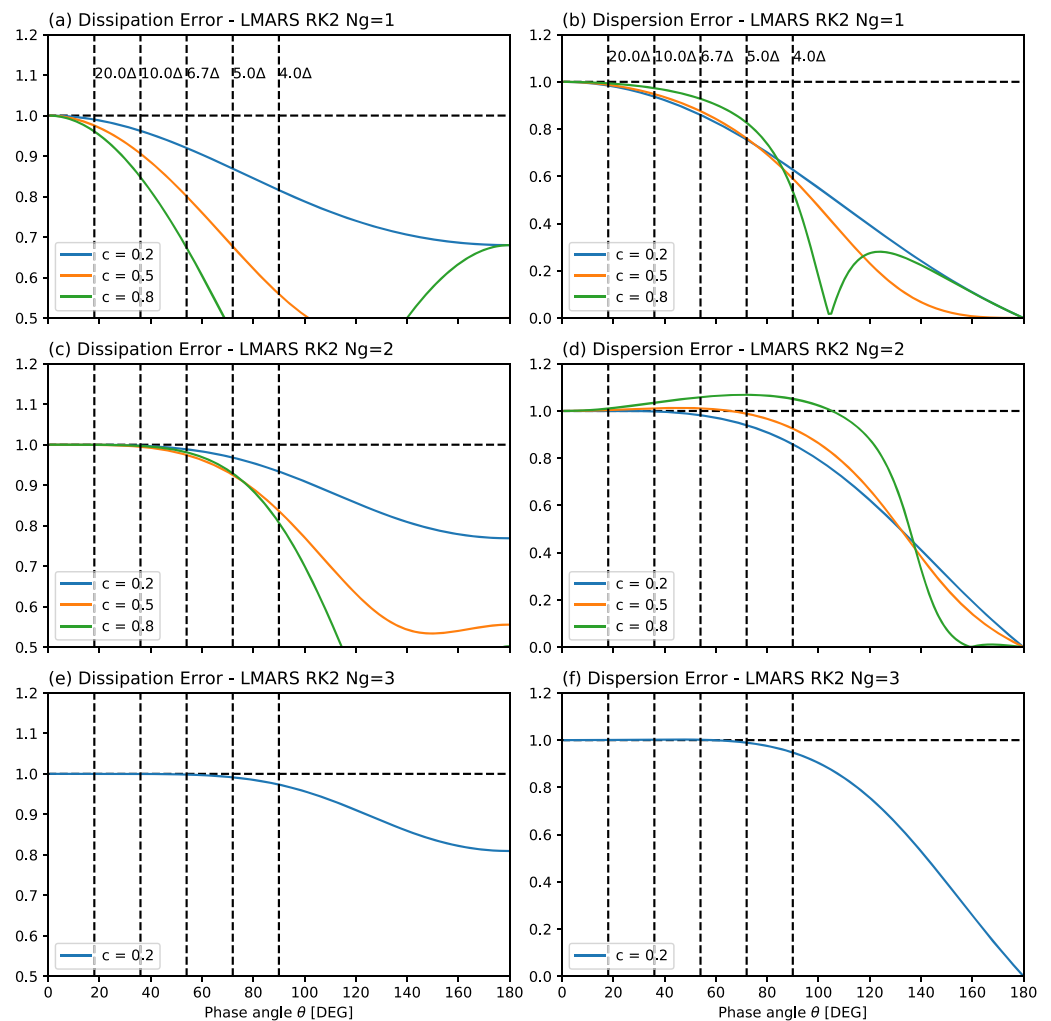
Figure A1. The dissipation (left column) and dispersion (right column) errors of the two-step Runge-Kutta Riemann-solver schemes with 3-point stencil ($N_g = 1$, row 1), 5-point stencil ($N_g = 2$, row 2), and 7-point stencil ($N_g = 3$, row 3). The vertical dashed lines are the corresponding phase angles to wave lengths of $4\Delta x$, $5\Delta x$, $6\frac{2}{3}\Delta x$, $10\Delta x$, and $20\Delta x$.

$$u_j^* = u_j^n - \frac{c}{2a} \sum_l A^{(l)} \phi_{j+l}^n + \frac{1}{2} c \sum_l C_{vmRS}^{(l)} u_{j+l}^n \tag{A2}$$

$$\phi_j^{n+1} = \phi_j^n - ac \sum_l A^{(l)} u_{j+l}^* + c \sum_l C_{vmRS}^{(l)} \phi_{j+l}^* \tag{A3}$$

$$u_j^{n+1} = u_j^n - \frac{c}{a} \sum_l A^{(l)} \phi_{j+l}^* + c \sum_l C_{vmRS}^{(l)} u_{j+l}^* \tag{A4}$$

which can be rewritten by

$$L_1 \begin{bmatrix} \phi \\ u \end{bmatrix}_{j+l}^* = R_1 \begin{bmatrix} \phi \\ u \end{bmatrix}_{j+l}^n \tag{A5}$$

$$L_2 \begin{bmatrix} \phi \\ u \end{bmatrix}_{j+l}^{n+1} = R_2 \begin{bmatrix} \phi \\ u \end{bmatrix}_{j+l}^n + R_2^* \begin{bmatrix} \phi \\ u \end{bmatrix}_{j+l}^* = \left(R_2 + R_2^* L_1^{-1} R_1 \right) \begin{bmatrix} \phi \\ u \end{bmatrix}_{j+l}^n \tag{A6}$$

where

$$L_1 = L_2 = L_1^{-1} = L_2^{-1} = \begin{bmatrix} 1 & 0 \\ 0 & 1 \end{bmatrix} \tag{A7}$$

$$R_1 = \begin{bmatrix} 1 & 0 \\ 0 & 1 \end{bmatrix} + \frac{1}{2} \sum_l \begin{bmatrix} cC_{vmRS}^{(l)} & -acA^{(l)} \\ -\frac{c}{a}A^{(l)} & cC_{vmRS}^{(l)} \end{bmatrix} \exp(il\theta) \tag{A8}$$

$$R_2 = \begin{bmatrix} 1 & 0 \\ 0 & 1 \end{bmatrix} \tag{A9}$$

$$R_2^* = \sum_l \begin{bmatrix} cC_{vmRS}^{(l)} & -acA^{(l)} \\ -\frac{c}{a}A^{(l)} & cC_{vmRS}^{(l)} \end{bmatrix} \exp(il\theta) \tag{A10}$$

then the amplification factor G is the eigenvalue of P, where

$$P = L_2^{-1} \left(R_2 + R_2^* L_1^{-1} R_1 \right) = R_2 + R_2^* R_1 \tag{A11}$$

The maximum allowed CFL numbers are $c_{max} = 0.9998$ for $N_g = 1$; $c_{max} = 0.92$ for $N_g = 2$; and $c_{max} = 0.49$ for $N_g = 3$. The maximum allowed CFL number of LMARS RK2 scheme with $N_g = 3$ is significantly limited to about 0.5, which is not competitive. The numerical estimation of the dissipation and dispersion errors are shown in Figure A1.

References

Abdi, D. S., & Giraldo, F. X. (2016). Efficient construction of unified continuous and discontinuous Galerkin formulations for the 3D Euler equations. *Journal of Computational Physics*, *320*, 46–68. https://doi.org/10.1016/j.jcp.2016.05.033

Arakawa, A., & Lamb, V. R. (1977). Computational design of the basic dynamical processes of the UCLA general circulation model. *Methods in Computational Physics*, *17*, 173–265.

Chen, X., Andronova, N., Van Leer, B., Penner, J. E., Boyd, J. P., Jablonowski, C., & Lin, S.-J. (2013). A Control-Volume Model of the Compressible Euler Equations with a Vertical Lagrangian Coordinate. *Monthly Weather Review*, *141*(7), 2526–2544. https://doi.org/10.1175/MWR-D-12-00129.1

Colella, P., & Woodward, P. R. (1984). The Piecewise Parabolic Method (PPM) for gas-dynamical simulations. *Journal of Computational Physics*, *54*(1), 174–201. https://doi.org/10.1016/0021-9991(84)90143-8

Eldred, C., & Le Roux, D. Y. (2018). Dispersion analysis of compatible Galerkin schemes for the 1D shallow water model. *Journal of Computational Physics*, *371*, 779–800. https://doi.org/10.1016/j.jcp.2018.06.007

Giraldo, F. X. (2014). Continuous and discontinuous Galerkin methods for atmospheric modeling. In *Seminar on Recent Developments in Numerical Methods for Atmosphere and Ocean Modelling, 2-5 September 2013*. Shinfield Park, Reading: ECMWF. Retrieved from https://www.ecmwf.int/en/learning/workshops-and-seminars/past-workshops/2013-annual-seminar, https://www.ecmwf.int/sites/default/files/elibrary/2014/9601-continuous-and-discontinuous-galerkin- methods-atmospheric-modeling.pdf

Giraldo, F. X., & Restelli, M. (2008). A study of spectral element and discontinuous Galerkin methods for the Navier-Stokes equations in nonhydrostatic mesoscale atmospheric modeling: Equation sets and test cases. *Journal of Computational Physics*, *227*(8), 3849–3877. https://doi.org/10.1016/j.jcp.2007.12.009

Godunov, S. K. (1959). A difference method for numerical calculation of discontinuous solutions of the equations of hydrodynamics. *Mat. Sb. (N.S.)*, *47*(89), (3), 271–306. Retrieved from http://www.mathnet.ru/php/archive.phtml?wshow=paper&jrnid=sm&paperid=4873&option_lang=eng

Harris, L. M., & Durran, D. R. (2010). An idealized comparison of one-way and two-way grid nesting. *Monthly Weather Review*, *138*(6), 2174–2187. https://doi.org/10.1175/2010MWR3080.1

Harris, L. M., & Lin, S.-J. (2013). A two-way nested global-regional dynamical core on the cubed-sphere grid. *Monthly Weather Review*, *141*(1), 283–306. https://doi.org/10.1175/MWR-D-11-00201.1

Harris, L. M., Lin, S.-J., & Tu, C. (2016). Hi gh-resolution climate simulations using GFDL HiRAM with a stretched global grid. *Journal of Climate*, *29*(11), 4293–4314. https://doi.org/10.1175/JCLI-D-15-0389.1

Harten, A., Lax, P. D., & van Leer, B. (1997). On upstream differencing and Godunov-type schemes for hyperbolic conservation laws. In M. Y. Hussaini, B. van Leer, & J. Van Rosendale (Eds.), *Upwind and High-Resolution Schemes* (pp. 53–79). Berlin, Heidelberg: Springer. https://doi.org/10.1007/978-3-642-60543-7_4

Hirsch, C. (2007). *Numerical Computation of Internal and External Flows: The Fundamentals of Computational Fluid Dynamics* (pp. 680). Oxford: Butterworth-Heinemann.

Katta, K. K., Nair, R. D., & Kumar, V. (2014). High-order finite-volume transport on the cubed sphere: Comparison between 1D and 2D reconstruction schemes. *Monthly Weather Review*, *143*(7), 2937–2954. https://doi.org/10.1175/MWR-D-13-00176.1

Kelly, J. F., & Giraldo, F. X. (2012). Continuous and discontinuous Galerkin methods for a scalable three-dimensional nonhydrostatic atmospheric model: Limited-area mode. *Journal of Computational Physics*, *231*(24), 7988–8008. https://doi.org/10.1016/j.jcp.2012.04.042

Kent, J., Whitehead, J. P., Jablonowski, C., & Rood, R. B. (2014). Determining the effective resolution of advection schemes. Part I: Dispersion analysis. *Journal of Computational Physics*, *278*, 485–496. https://doi.org/10.1016/j.jcp.2014.01.043

Kopera, M. A., & Giraldo, F. X. (2014). Analysis of adaptive mesh refinement for IMEX discontinuous Galerkin solutions of the compressible Euler equations with application to atmospheric simulations. *Journal of Computational Physics*, *275*, 92–117. https://doi.org/10.1016/j.jcp.2014.06.026

Lauritzen, P. H. (2007). A stability analysis of finite-volume advection schemes permitting long time steps. *Monthly Weather Review*, *135*(7), 2658–2673. https://doi.org/10.1175/MWR3425.1

Lin, S.-J. (2004). A "Vertically Lagrangian" finite-volume dynamical core for global models. *Monthly Weather Review*, *132*(10), 2293–2307. https://doi.org/10.1175/1520-0493(2004)132<2293:AVLFDC>2.0.CO;2

Lin, S.-J., & Rood, R. B. (1996). Multidimensional flux-form semi-Lagrangian transport schemes. *Monthly Weather Review*, *124*(9), 2046–2070. https://doi.org/10.1175/1520-0493(1996)124<2046:MFFSLT>2.0.CO;2

Liou, M.-S. (2006). A sequel to AUSM, Part II: AUSM+-up for all speeds. *Journal of Computational Physics*, *214*(1), 137–170. https://doi.org/10.1016/j.jcp.2005.09.020

Mesinger, F. (1977). Forward-backward scheme, and its use in a limited area model. *Contributions to Atmospheric Physics*, *50*, 200–210. Retrieved from https://www.researchgate.net/publication/284037366_Forward-backward_scheme_and_its_use_in_a_limited_area_model

Randall, D. A. (1994). Geostrophic adjustment and the finite-difference shallow-water equations. *Monthly Weather Review*, *122*(6), 1371–1377. https://doi.org/10.1175/1520-0493(1994)122<1371:GAATFD>2.0.CO;2

Roe, P. L. (1981). Approximate Riemann solvers, parameter vectors, and difference schemes. *Journal of Computational Physics*, *43*(2), 357–372. https://doi.org/10.1016/0021-9991(81)90128-5

Shu, C.-W., & Osher, S. (1988). Efficient implementation of essentially non-oscillatory shock-capturing schemes. *Journal of Computational Physics*, *77*(2), 439–471. https://doi.org/10.1016/0021-9991(88)90177-5

Skamarock, W. C. (2008). A linear analysis of the NCAR CCSM finite-volume dynamical core. *Monthly Weather Review*, *136*(6), 2112–2119. https://doi.org/10.1175/2007MWR2217.1

Staniforth, A., Melvin, T., & Cotter, C. (2013). Analysis of a mixed finite-element pair proposed for an atmospheric dynamical core. *Quarterly Journal of the Royal Meteorological Society*, *139*(674), 1239–1254. https://doi.org/10.1002/qj.2028

Ullrich, P. A. (2014). Understanding the treatment of waves in atmospheric models. Part 1: The shortest resolved waves of the 1D linearized shallow-water equations. *Quarterly Journal of the Royal Meteorological Society*, *140*(682), 1426–1440. https://doi.org/10.1002/qj.2226

Ullrich, P. A., & Jablonowski, C. (2011). An analysis of 1D finite-volume methods for geophysical problems on refined grids. *Journal of Computational Physics*, *230*(3), 706–725. https://doi.org/10.1016/j.jcp.2010.10.014

Ullrich, P. A., & Jablonowski, C. (2012). MCore: A non-hydrostatic atmospheric dynamical core utilizing high-order finite-volume methods. *Journal of Computational Physics*, *231*(15), 5078–5108. https://doi.org/10.1016/j.jcp.2012.04.024

Ullrich, P. A., Jablonowski, C., & van Leer, B. (2010). High-order finite-volume methods for the shallow-water equations on the sphere. *Journal of Computational Physics*, *229*(17), 6104–6134. https://doi.org/10.1016/j.jcp.2010.04.044

van Leer, B. (1974). Towards the ultimate conservative difference scheme. II. Monotonicity and conservation combined in a second-order scheme. *Journal of Computational Physics*, *14*(4), 361–370. https://doi.org/10.1016/0021-9991(74)90019-9

van Leer, B. (1979). Towards the ultimate conservative difference scheme. V. A second-order sequel to Godunov's method. *Journal of Computational Physics*, *32*(1), 101–136. https://doi.org/10.1016/0021-9991(79)90145-1

Weller, H., Lock, S.-J., & Wood, N. (2013). Runge-Kutta IMEX schemes for the horizontally explicit/vertically implicit (HEVI) solution of wave equations. *Journal of Computational Physics*, *252*, 365–381. https://doi.org/10.1016/j.jcp.2013.06.025

Yang, C., Cao, J., & Cai, X.-C. (2010). A fully implicit domain decomposition algorithm for shallow water equations on the cubed-sphere. *SIAM Journal on Scientific Computing*, *32*(1), 418–438. https://doi.org/10.1137/080727348